Journal of Power Sources 195 (2010) 4871–4892

Contents lists available at ScienceDirect

Journal of Power Sources

journal homepage: www.elsevier.com/locate/jpowsour

A multi-level simulation platform of natural gas internal reforming solid oxide fuel cell–gas turbine hybrid generation system: Part I. Solid oxide fuel cell model library

Cheng Bao[a,b,*], Yixiang Shi[b], Eric Croiset[b,c], Chen Li[b], Ningsheng Cai[b]

[a] Department of Thermal Science and Energy Engineering, School of Mechanical Engineering, University of Science & Technology Beijing, Beijing 100083, PR China
[b] Key Laboratory for Thermal Science and Power Engineering of Ministry of Education, Tsinghua University, Beijing 100084, PR China
[c] Department of Chemical Engineering, University of Waterloo, Waterloo, Ontario N2L 3G1, Canada

ARTICLE INFO

Article history:
Received 21 January 2010
Accepted 27 January 2010
Available online 4 February 2010

Keywords:
Solid oxide fuel cell
Natural gas
Multi-level simulation platform
Distributed model
Radiation heat transfer
Analytical view factor

ABSTRACT

In this paper, a hierarchical model library of natural gas internal reforming (IR) solid oxide fuel cells (SOFCs) is developed to reflect a multi-level modeling design. First, two types of positive electrolyte negative (PEN) models are presented, which take into account the electromotive force of multi-component fuel and H_2/CO joint electrochemical oxidation. Secondly, an advanced PEN model is introduced for better prediction at high fuel utilization. Thirdly, an approximate analytical PEN model is introduced to achieve a balance between accuracy and speed. Cell-level modeling provides boundary conditions for PEN-level models via a unified description of flow and heat transfer in both planar and tubular geometries. Unlike quasi-equilibrium and lumped cell-level models, distributed modeling reveals a significant difference between outlet gas temperatures and average solid temperature, especially under countercurrent flow. Based on analytical view factors, the detailed radiation heat transfer model shows greater uniform distribution of current density and solid temperature. Upon validation, the multi-level SOFC model library constitutes the main component of the modular simulation platform for IRSOFC–GT (gas turbine) hybrid generation systems in a gPROMS environment.

1. Introduction

Fuel cells are a kind of clean and efficient power source that directly converts the chemical energy of fuel into electricity. With high-quality exhaust energy and considerable fuel flexibility, a solid oxide fuel cell (SOFC) can be combined with a gas turbine (GT) to form a SOFC–GT hybrid generation system, which is considered to be the best candidate for the distributed power system, power station, vehicular auxiliary power unit, and optimization of other efficient energy technologies.

Modeling and simulation play an important role in the development of SOFC–GT hybrid generation technology. Solid oxide fuel cells contain complex phenomena of gas flow, electrochemical reaction, mass/charge transfer and convective/radiant heat transfer. Meanwhile, different cell structures of the planar, tubular and flat tubular geometries create other problems, such as the radial and circumferential conductions of current paths in the tubular SOFCs. When hydrocarbon fuel (e.g. natural gas) is utilized, chemical reactions occur in the anode, including internal reforming ($CH_4 + H_2O \rightarrow 3H_2 + CO$), water gas shift ($CO + H_2O \rightarrow H_2 + CO_2$) and even methane cracking and coke formation. Based on multi-physics governing equations, mathematical modeling has been widely applied for cell design and performance prediction to reduce experimental costs.

In recent years, there has been an extensive literature about electrode-level and cell-level modeling and analysis. Besides semi-empirical models, state-of-the-art mechanistic models of solid oxide fuel cells have been developed for multi-dimensional, non-isothermal, transient modeling using computational fluid dynamics (CFD) technology [1]. These models provide a good understanding of the principle of SOFCs. Most are homogeneous, because their electrochemical models generally focus on the overall mass/charge transfer and polarization. Other literature focuses on the detailed reaction mechanisms of hydrogen oxidation or oxygen reduction in the porous electrodes [2,3]. Although these heterogeneous cell models are very complicated for cell-level and system-level analysis, some of their mechanisms (e.g. surface diffusion and competition absorption) have provided useful information that guarantees the accuracy of the user models developed in this study.

* Corresponding author at: Department of Thermal Science and Energy Engineering, School of Mechanical Engineering, University of Science & Technology Beijing, No. 30 XueYuan Road, Haidian Zone, Beijing 100083, PR China.
Tel.: +86 10 62333682; fax: +86 10 62329145.
E-mail address: baocheng@mail.tsinghua.edu.cn (C. Bao).

0378-7753/$ – see front matter © 2010 Elsevier B.V. All rights reserved.
doi:10.1016/j.jpowsour.2010.01.078

Nomenclature

A	area (m^2)
B	radiosity of surface ($W\,m^{-2}$)
c	concentration ($mol\,m^{-3}$)
c_f	Colburn friction factor
c_p	mass specific heat ($J\,kg^{-1}\,K^{-1}$)
C_p	molar specific heat ($J\,mol^{-1}\,K^{-1}$)
D	diffusivity ($m^2\,s$) or diameter (m) or depth (m)
E	activation energy for electrochemical reaction ($J\,mol^{-1}$)
F	Faraday's constant ($96487\,C\,mol^{-1}$) or view factor
H	molar enthalpy ($J\,mol^{-1}$)
i_0	exchange current density ($A\,m^{-2}$)
i	local current density ($A\,m^{-2}$)
I	current density ($A\,m^{-2}$)
j	electrochemical reaction rate ($A\,m^{-3}$)
J	current (A)
K_{eq}	equilibrium constant (bar^2 or 1)
L	cell length (m)
M	molecular weight ($kg\,mol^{-1}$)
n_e	electrons transferred per reacting molecule
N	flux ($mol\,m^{-2}\,s^{-1}$)
p	pressure (Pa)
q	radiation flux of element surface ($W\,m^{-2}$)
Q	activation energy for surface adsorption ($J\,mol^{-1}$)
r	radius (m) or volumetric reaction rate ($mol\,m^{-3}\,s^{-1}$)
R	reaction rate per area ($mol\,m^{-2}\,s^{-1}$) or resistivity ($\Omega\,m$)
$\Re$	universal gas constant ($8.314\,J\,mol^{-1}\,K^{-1}$)
S	specific area per unit volume ($m^2\,m^{-3}$)
T	temperature (K)
u	velocity ($m\,s^{-1}$)
V	volume (m^3) or voltage (V)
W	width (m)
x	molar fraction or coordinate in thickness direction (m)
z	coordinate in the cell length thickness (m)
X, Y, Z	dimensionless parameters for view factors

Greek

α	anodic transfer coefficient or activity
β	cathodic transfer coefficient
δ	thickness (m)
ε	electrode porosity or perturbation variable
η	overpotential (V)
$\in$	emissivity
γ	reaction order
κ	heat conductivity ($W\,m^{-1}\,K^{-1}$)
ϕ	potential (V)
ψ, ψ_{INT}, ψ_P	switching coefficients for different cases
ρ	density ($kg\,m^{-3}$)
σ	conductivity ($S\,m^{-1}$)
τ	electrode tortuosity
θ, Θ	absolute and relative surface coverage
υ	stoichiometric coefficient of reaction
ζ	friction coefficient or rib coefficient

Subscripts and superscripts

a	anode
AST	air supply tube
c	cathode
CON	interconnector
e	electrolyte
eff	effective
el	electronic conducting phase
eq	equilibrium
i, j	species
in	inlet or inner
ion	ionic conducting phase
out	outlet or outer
PEN	positive electrolyte negative
ref	reference or reforming reaction
t	total or overall
TPB	triple phase boundary
WGS	water gas shift reaction

In addition to solid oxide fuel cells, there are other balancing units in SOFC–GT hybrid systems, such as the gas turbine, reformer, heat exchanger, ejector, burner, splitter, mixer, etc. System-level modeling and thermodynamic analysis generally focus on the effects of operational conditions on full-load and part-load system performance, which includes the gas flow rate, cell temperature, reactants recirculation, internal reforming, radiation heat transfer, stack stage, afterburner, fixed-speed and variable-speed control strategy of gas turbines, etc. [1].

Fig. 1 shows our research idea for modeling and control of a natural gas internal reforming (IR) SOFC–GT hybrid generation system. A SOFC–GT simulation platform has been developed based on model libraries of the main system units, including the SOFC, GT, reformer, heat exchanger, ejector, etc. [4]. The platform aims at system optimization, dynamics analysis and controller design, and hardware-in-the-loop simulation. Various system configurations and numerical requirements call for multi-level unit models of different complexity [5]. The purpose of this paper is to present a multi-level model library of the core component SOFC. For system-level analysis, the complex CFD-based numeration and detailed models of elementary pathway were avoided in the SOFC modeling. However, compared to most system-level thermodynamic models, the SOFC modeling improved on important aspects, including the transport phenomena in positive electrolyte negative (PEN), radiation heat transfer, parameter distribution, dynamic performance, etc. Moreover, an appropriate numerical environment is also important for modular simulation of different system configurations.

In PEN-level modeling, a general PEN model was first presented by taking H_2/CO joint electrochemical oxidation and the electromotive force of multi-component fuel into account. Further, an approximate analytical solution of the general PEN model was developed to provide a balance between accuracy and fast calculation. An advanced PEN model was presented to introduce the mechanism of surface diffusion and competition absorption. In cell-level modeling, a pseudo-2D distributed model including detailed radiant heat transfer was developed to achieve better prediction of cell performance than quasi-equilibrium and lumped modeling. In a gPROMS commercial environment, all levels of models were graphically specified, allowing users to flexibly deploy their SOFC models in different cases.

2. Equation-oriented gPROMS environment

To date, there have been many computer-based models for simulating chemical process plants and power plants, such as commercially available Hysys, Aspen, Pro II, ThermoFlex, GATE/Cycle, etc. However, with the exception of simple thermodynamic analysis, most of these models have little capability for detailed modeling

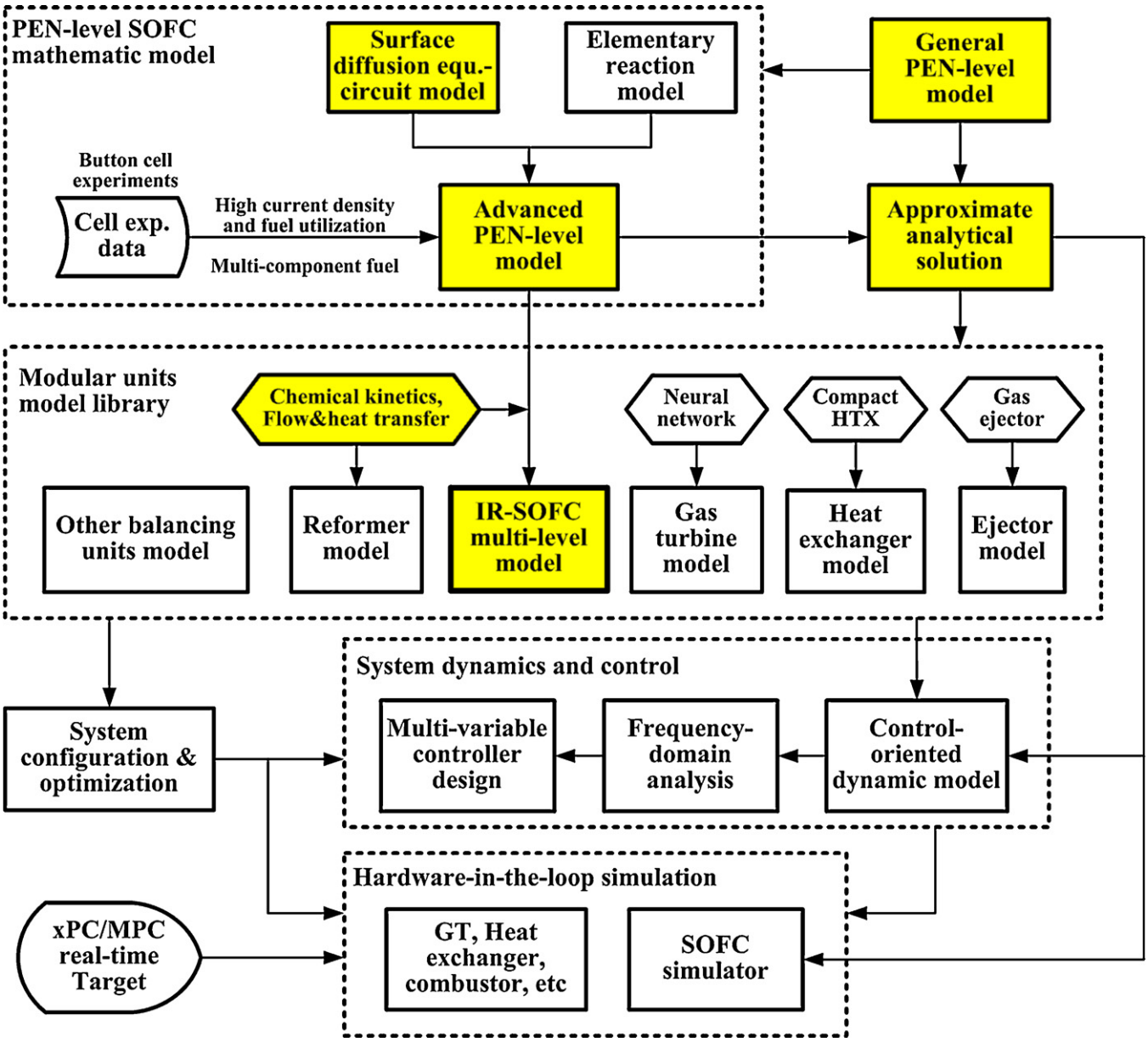

Fig. 1. Research idea of modeling and control of IRSOFC–GT hybrid generation system.

of fuel cells. In addition, it is also difficult to model in detail all the balancing units in one of these models. For this reason, specific analytical tools were developed for the SOFC-based power system [6].

Matlab, with its strong numeration and optimization toolboxes, is also a good mathematical tool for modeling SOFC–GT power cycles. Furthermore, it can be seamlessly combined with COMSOL, a commercial tool for finite element analysis. However, a low numerical efficiency and sequential-solving approach limits its application for complex analysis. There are a few control-oriented models of high-temperature fuel cells in a Matlab environment [7,8].

The multi-level SOFC–GT simulation platform in this paper was developed based on the commercial advanced process modeling environment, gPROMS [9]. The characteristics of gPROMS include: (1) built-in models and abundant physical properties, (2) easy gPROMS language for independent programming, (3) simultaneous operation of lumped and distributed models, (4) integrated environmental modeling, optimization and control design, (5) fast and robust numerical algorithms, (6) optional interfaces with Matlab, Aspen, etc., (7) object-oriented and hierarchical modeling designs, similar to the human thinking process, and (8) graphic specification for modular modeling and configuration. There have been a few gPROMS-based models of SOFC–GT hybrid generation systems [10,11].

Most importantly, the equation-oriented solver of gPROMS is very suitable for modeling fuel cells. As shown in Fig. 2, there are two methods in the distributed modeling of the voltage–current performance of fuel cells: one is to provide operating voltage and the other is to provide operating current density. In distributed modeling, the fuel cell is generally thought of as a set of parallel discrete elements with uniform cell voltage (i.e. cell operating voltage) and non-uniform local current densities. Thus, besides the governing differential equations of flow, heat transfer and chemical/electrochemical reaction for every cell element, there is an outer algebraic loop for the iteration of cell voltage or average current density. For the sequential-solving approach, this iteration loop increases the time taken toe achieve a result and reduces

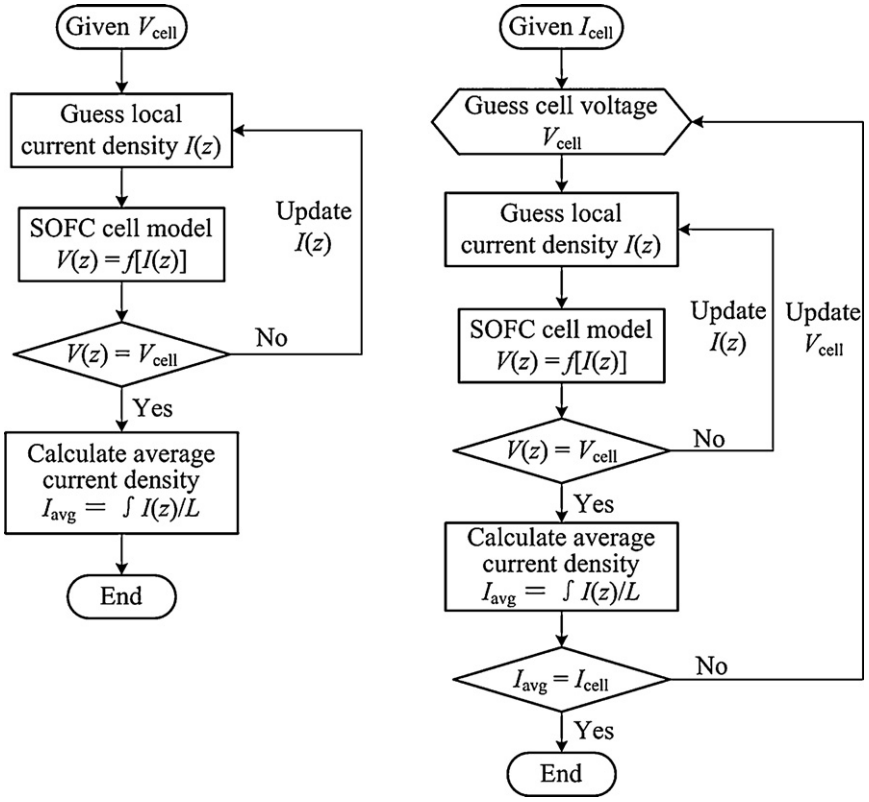

Fig. 2. Flow chart showing the calculation of cell performance with voltage–current iteration loop.

the possibility of convergence. With the equation-oriented solver in gPROMS, the constraint of uniform voltage ($V(z) = const$) can be directly included in the governing equations. Compared to the Matlab code based on its partial differential equation toolbox (Pdepe) [12], the gPROMS code without the outer iteration loop provides a much faster and more stable performance. However, this equation-oriented solver also requires more debugging skills.

3. Unified description for planar and tubular SOFC

Fig. 3 shows the schematic diagram of a section of planar and tubular SOFCs. For the rectangular flow channels of planar SOFCs (PSOFC), W_{ch} and W_{rib} are the width of the flow channel and rib, D_a and D_c are the depth of the anode and cathode flow channel, n_{ch} is the number of flow channels, $A_{CON} = A_{CON,a} + A_{CON,c}$ is the total section area of interconnector (CON). For tubular SOFCs (TSOFC), the fuel flows along the outside of tube, while the air is first preheated via the air supply tube (AST) and then flows back into the annular area between the cathode and the air supply tube. Here, $r_{AST,in}$ and $r_{AST,out}$ are the inner and outer radius of the AST, r_{in} and r_{out} are the inner and outer radius of the cell tube, r_{ea} and r_{ec} are the radius of the electrolyte/anode and electrolyte/cathode interface, δ_a, δ_c and δ_e are the thickness of the anode, cathode and electrolyte layer, respectively, $\delta_{PEN} = \delta_a + \delta_c + \delta_e$ is the PEN thickness, L is the cell tube length, and δ_t is the tube spacing in a bank of cell tubes. In order to describe PSOFCs and TSOFCs as a set of unified governing equations, it is necessary to define some geometry-related parameters as follows:

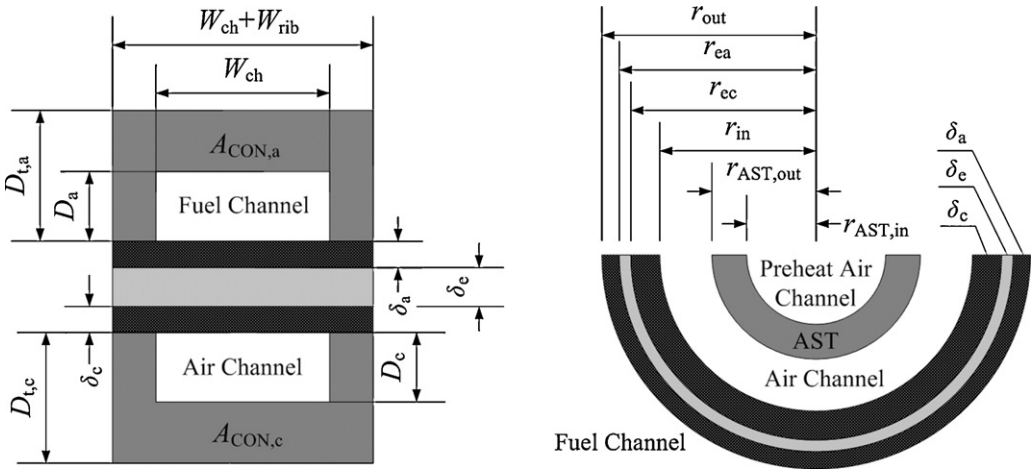

Fig. 3. The schematic diagram of the section in planar and tubular SOFCs.

(1) With the given solid-phase density (ρ_s), mass specific heat ($c_{p,s}$), heat conductivity (κ_s) and porosity (ε) of the anode (subscript or superscript as 'a'), the cathode (c) and the electrolyte (e), the corresponding property of PEN can be obtained by:

$$\rho_{PEN}=\varphi_a\rho_{a,s}+\varphi_c\rho_{c,s}+\varphi_e\rho_{e,s},\quad \kappa_{PEN}=\varphi_a\kappa_{a,s}+\varphi_c\kappa_{c,s}+\varphi_e\kappa_{e,s}$$
$$c_{p,PEN}=\frac{(\varphi_a\rho_{a,s}c^a_{p,s}+\varphi_c\rho_{c,s}c^c_{p,s}+\varphi_e\rho_{e,s}c^e_{p,s})}{\rho_{PEN}} \quad (1)$$

where φ_a, φ_c, φ_e are the volumetric fraction of the corresponding layer in PEN. Assuming a dense electrolyte layer (i.e. $\varepsilon_e = 0$) for PSOFC,

$$\varphi_k=\frac{\delta_k(1-\varepsilon_k)}{\sum_{k=a,c,e}\delta_k(1-\varepsilon_k)} \quad (2)$$

for TSOFC,

$$\varphi_k=\frac{(r^2_{k,out}-r^2_{k,in})(1-\varepsilon_k)}{\sum_{k=a,c,e}(r^2_{k,out}-r^2_{k,in})(1-\varepsilon_k)} \quad (3)$$
$$r_{a,out}=r_{out},\quad r_{a,in}=r_{e,out}=r_{ea},\quad r_{c,out}=r_{e,in}=r_{ec},\quad r_{c,in}=r_{in}$$

With the given density (ρ_{CON}) and mass specific heat ($c_{p,CON}$) of the interconnector, the heat capacity of the total solid phase in PSOFC is

$$\rho_s c_{p,s}V_s=n_{ch}L[(W_{ch}+W_{rib})\delta_{PEN}\rho_{PEN}c_{p,PEN}+A_{CON}\rho_{CON}c_{p,CON}] \quad (4)$$

With the given density (ρ_{AST}) and mass specific heat ($c_{p,AST}$) of the air supply tube in TSOFC,

$$\rho_s c_{p,s}V_s=L[(r^2_{out}-r^2_{in})\rho_{PEN}c_{p,PEN}+(r^2_{AST,out}-r^2_{AST,in})\rho_{AST}c_{p,AST}] \quad (5)$$

(2) When considering the existence of the rib, the rib coefficient is defined as $\zeta_{rib} = 1 + W_{rib}/W_{ch}$ in PSOFC. In TSOFC, there is no rib, i.e. $\zeta_{rib} = 1$. For PSOFC, the effective area of mass transfer and the volume of the anode and cathode flow channel are:

$$A_a=A_c=n_{ch}W_{ch}\zeta_{rib}L,\quad V_a=n_{ch}W_{ch}D_aL,\quad V_c=n_{ch}W_{ch}D_cL \quad (6)$$

For TSOFC,

$$A_a=2\pi r_{out}L,\quad V_a=[(\delta_t+2r_{out})^2-\pi r^2_{out}]L$$
$$A_c=2\pi r_{in}L,\quad V_c=\pi(r^2_{in}-r^2_{AST,out}+r^2_{AST,in})L \quad (7)$$

For the unit volume of flow channel in PSOFC, the convective heat transfer area between the gaseous and solid phases is:

$$S_{k,PEN}=\frac{1}{D_k},\quad S_{k,CON}=\frac{(2D_k+W_{ch})}{(D_kW_{ch})}\quad (k = a, c) \quad (8)$$

For TSOFC,

$$S_{a,PEN}=\frac{2\pi r_{out}}{(\delta_t+2r_{out})^2-\pi r^2_{out}}$$
$$S_{c,PEN}=\frac{2r_{in}}{(r^2_{AST,out}-r^2_{in})},\quad S_{AST}=\frac{2r_{AST,out}}{(r^2_{AST,out}-r^2_{in})} \quad (9)$$

For PSOFC, the effective mass transfer area (subscript as '*m*') and the heat transfer area (*h*) per unit volume of PEN is:

$$S_{m,PEN,k}=\frac{1}{\delta_{PEN}},\quad S_{h,PEN,k}=\frac{1}{(\zeta_{rib}\delta_{PEN})}\quad (k = a, c) \quad (10)$$

For TSOFC,

$$S_{m,PEN,a}=S_{h,PEN,a}=\frac{2r_{out}}{(r^2_{out}-r^2_{in})},$$
$$S_{m,PEN,c}=S_{h,PEN,c}=\frac{2r_{in}}{(r^2_{out}-r^2_{in})} \quad (11)$$

(3) For the rectangle flow channel of PSOFC, the hydraulic diameter (D_e) is:

$$D_{e,a}=\frac{2W_{ch}D_a}{W_{ch}+D_a},\quad D_{e,c}=\frac{2W_{ch}D_c}{W_{ch}+D_c} \quad (12)$$

For the circular or annular flow channel of TSOFC,

$$D_{e,a}=2r_{out},\quad D_{e,c}=2(r_{in}-r_{AST,out}) \quad (13)$$

4. IRSOFC multi-level models

In this research the multi-level modeling concept was fully reflected in the hierarchical models of the natural gas internal reforming solid oxide fuel cells (IRSOFC). There were PEN-level, cell-level, and system-level models in the IRSOFC model library. The PEN-level models were isothermal and focused on the mass/charge transfer and electrochemical/chemical reactions in PEN. Since PEN thickness is generally much less than the cell length, it is reasonable to neglect the temperature gradient along the direction of the PEN thickness. In general, the dynamic PEN models were used for electrochemical impedance spectroscopy (EIS) analysis [13]. Compared to the dominant system transient behaviors (i.e. dynamics of mechanical inertia, volume filling of gas flow, variation of solid temperature, etc.), the dynamics of transport phenomena in PEN is fast enough to be neglected. Therefore, the PEN-level models were steady-state in this paper. Assuming that the electrochemical and chemical reactions occur everywhere in the electrodes or only at two sides of the electrodes, the PEN models could be divided into control volume type models and interface-type models. As a result of gas flow and heat transfer, parameter distribution and transient behaviors were further investigated in cell-level models, which were divided into quasi-equilibrium, lumped and distributed cell-level models. Under different cell structures and gas flow modes, the cell-level model exchanged boundary conditions (i.e. gas pressure, species bulk concentrations, local cell temperature, cell voltage, or local current density) at the flow channel/electrode interface with the PEN-level models. Neglecting the difference among cells, the cell-level models could be easily extended for system-level analysis. For the natural gas internal reforming, H_2–H_2O–CO–CO_2–CH_4–N_2 mixture and air were taken as fuel and oxidant, respectively, in all the SOFC models. Table 1 describes the functions, assumptions and limitations of each model.

4.1. PEN-level model

As shown in Fig. 4, the core of SOFC is a "sandwich" structure of PEN. The electrolyte is made from a ceramic, such as yttria-stabilized zirconia (YSZ), to conduct oxygen ions and separate

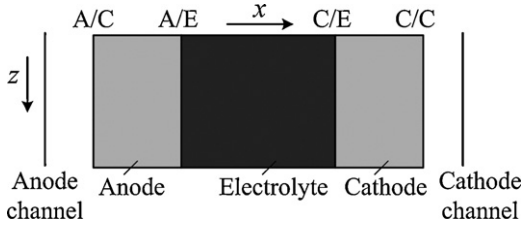

Fig. 4. Pesudo-2D schematic diagram of SOFCs.

Table 1
Characteristics of different SOFC models.

Level	Type	Functions, assumptions and limitations
PEN-level	Control volume (CV-) type	Electrochemical and chemical reactions occur everywhere, isothermal, steady-state and one-dimensional model, compatible with general or advanced PEN model
	Interface (INT-) type	Chemical reactions occur at anode/channel interface, electrochemical reactions occur at electrode/electrolyte interface, isothermal, steady-state and one-dimensional model, compatible with general or advanced PEN model
	Approximate analytical solution	Approximation of CV-type general PEN model with binary reactants, especially suitable for control-oriented analysis and hardware-in-the-loop simulation
	Advanced PEN model	Improvement at high fuel utilization by introduction of surface diffusion and competition absorption, keep the simple frame as general PEN model
Cell-level	Quasi-equilibrium	Steady-state model, reforming and WGS reactions are in equilibrium, the same temperature of outlet gases and solid phase, suitable for INT-type PEN-level model
	Lumped	CSTR dynamic model, the same temperature of outlet gases and solid phase, suitable for all PEN-level models
	Distributed	Distributed dynamic model, parameters distribution along length direction, detailed radiant heat transfer with analytical view factors, suitable for all PEN-level models
System-level	Identical to cell-level model	Neglect difference among cells, analysis of stack stage or stack network

reactants. The electrodes are formed by a mixture of ionic conductor and electronic conductor materials, and porosities are presented in the structure for gas diffusion and ion/electron transport to create the three phase boundary (TPB). The electrochemical reaction occurs at the TPB sites, which involves the oxidation of fuel ($H_2 + O^{2-} \rightarrow H_2O + 2e^-$, $CO + O^{2-} \rightarrow CO_2 + 2e^-$) in the anode and the reduction of oxygen ($1/2O_2 + 2e^- \rightarrow O^{2-}$) in the cathode, and the current density exchange between the ionic and electronic conducting phases. For hydrocarbon fuel (e.g. natural gas), there are also chemical reactions of internal reforming and water gas shift in the anode. The PEN-level transport model in this research was an isothermal, steady-state, one-dimensional model, in which only the x coordinate in the thickness direction of PEN was considered and moved positively along the x coordinate from the anode to the cathode.

4.1.1. Control volume type PEN model

In the control volume (CV-) type PEN model, electrochemical and chemical reactions occur everywhere at the TPBs. According to Ohm's law, the charge transfer in the electronic (el) and ionic (ion) conducting phases of the electrode is

$$x^{-m}\nabla\cdot(-x^m\sigma_{\text{ion}}^{\text{eff}}\nabla\phi_{\text{ion}}) = x^{-m}\nabla\cdot(x^m\sigma_{\text{el}}^{\text{eff}}\nabla\phi_{\text{el}}) = \sum_{\text{k=H}_2,\text{CO or O}_2}\psi j_{\text{k}} \tag{14}$$

which is suitable for both PSOFC ($m = 0$) and TSOFC ($m = 1$). Where ϕ and σ are the potential and conductivity ($\psi = 1$ in the anode and $\psi = -1$ in the cathode), respectively, the electrochemical reaction rate (H_2 and CO oxidation in the anode, oxygen reduction in the cathode), j, can be described by the general current–overpotential equation

$$j = i_0 S_{\text{TPB}}\left[\frac{c_{\text{react,TPB}}}{c_{\text{react,b}}}\exp\left(\frac{\alpha n_{\text{e}}F}{\Re T}\psi\eta\right) - \frac{c_{\text{prod,TPB}}}{c_{\text{prod,b}}}\exp\left(-\frac{\beta n_{\text{e}}F}{\Re T}\psi\eta\right)\right]$$
$$i_0 = i_{0,\text{ref}}\exp\left[-\frac{E}{\Re}\left(\frac{1}{T}-\frac{1}{T_{\text{ref}}}\right)\right]\Pi\left(\frac{p_i}{p_0}\right)^{\gamma_i} \tag{15}$$

where F is the Faraday constant, $\Re$ is the universal gas constant, T is the operating temperature, $n_e = 2$ is the number of electrons participating in the electrochemical reaction, α and β are the charge transfer coefficients, c_{TPB} and c_b are the TPB concentration and bulk concentration of reactants and products, respectively, S_{TPB} is the TPB active area per unit volume of electrode, $i_{0,\text{ref}}$ is the reference exchange current density at the reference temperature T_{ref}, E is the activation energy, p_i and γ_i are the partial pressure and reaction order of species i, and the overpotential η is defined as the potential difference between the two phases ($\phi_{\text{el}} - \phi_{\text{ion}}$) minus the potential difference in equilibrium, which is positive in the anode and negative in the cathode. In the electrolyte layer, there is a linear distribution of ionic phase potential, i.e. $\nabla^2\phi_{\text{ion}} = 0$.

The mass transfer in the porous electrode is described by the Stefan–Maxwell equation

$$\nabla x_i = \frac{\tau}{\varepsilon}\sum_{j\neq i}\frac{x_iN_j - x_jN_i}{c_{\text{t}}D_{ij}} - \frac{\tau}{\varepsilon}\frac{N_i}{c_{\text{t}}D_{i,\text{K}}}$$
$$(i = \text{H}_2, \text{H}_2\text{O}, \text{CO}, \text{CO}_2, \text{CH}_4, \text{N}_2, \text{O}_2) \tag{16}$$

where ε and τ are the electrode porosity and tortuosity, c_t is the concentration of gas mixture, $x_i = c_i/c_t$ and N_i are the molar fraction and diffusion flux of species i, respectively, D_{ij} is the binary diffusivity between gaseous species i and j, and $D_{i,K}$ is the Knudsen diffusion coefficient of species i.

The mass balance of species in the electrode is related to the electrochemical reaction rate

$$x^{-m}\nabla\cdot(x^mN_i) = \sum_{\text{k=H}_2,\text{CO or O}_2}\frac{\upsilon_{i,\text{k,elec}}j_{\text{k}}}{n_{\text{e}}F} + \upsilon_{i,\text{ref}}r_{\text{ref}} + \upsilon_{i,\text{WGS}}r_{\text{WGS}} \tag{17}$$

where $\upsilon_{i,\text{H}_2,\text{elec}} = [-1, 1, 0, 0, 0, 0, -0.5]$ and $\upsilon_{i,\text{CO,elec}} = [0, 0, -1, 1, 0, 0, -0.5]$ are the stoichiometric coefficients of species i in H_2 and CO electrochemical reactions, respectively. $\upsilon_{i,\text{ref}} = [3, -1, 1, 0, -1, 0, 0]$ and $\upsilon_{i,\text{WGS}} = [1, -1, -1, 1, 0, 0, 0]$ are the stoichiometric coefficients of species i in reforming and water gas shift (WGS) reactions, respectively. The kinetics (mol m^{-3} s^{-1}) in the Ni-YSZ cermet can be obtained by [14]

$$r_{\text{ref}} = 2395\exp\left(-\frac{231266}{\Re T}\right)\left(p_{\text{CH}_4}p_{\text{H}_2\text{O}} - \frac{p_{\text{CO}}p_{\text{H}_2}^3}{K_{\text{eq,ref}}}\right)$$
$$r_{\text{WGS}} = 0.0171\exp\left(-\frac{103191}{\Re T}\right)\left(p_{\text{CO}}p_{\text{H}_2\text{O}} - \frac{p_{\text{H}_2}p_{\text{CO}_2}}{K_{\text{eq,WGS}}}\right) \tag{18}$$

where the equilibrium constants $K_{\text{eq,ref}}$ and $K_{\text{eq,WGS}}$ are related to the operating temperature [14].

At the electrode/flow channel (E/C: A/C or C/C) interface, the species concentration is the bulk concentration and the ionic current is fully transferred to the electronic current. At the electrode/electrolyte (E/E: A/E or C/E) interface, the electronic current is fully transferred to the ionic current, and the dense electrolyte prevents species diffusion. Corresponding to the two calculation methods of cell performance, there are two kinds of boundary con-

ditions. When the operating current (J) is provided,

$$x_i|_{E/C}=x_{i,b},\ \sigma_{el}^{eff}\left.\frac{d\eta}{dx}\right|_{E/C}=-\frac{J}{A_{E/C}},\quad N_i|_{E/E}=0,\quad \sigma_{ion}^{eff}\left.\frac{d\eta}{dx}\right|_{E/E}=\frac{J}{A_{E/E}} \tag{19}$$

where $A_{E/C}$ and $A_{E/E}$ are the active areas at E/C and E/E interface, respectively. For PSOFC, $A_{A/C}=A_{C/C}=A_{E/E}=n_{ch}W_{ch}\zeta_{rib}L$. For TSOFC, $A_{A/C}=2\pi r_{out}L$, $A_{A/E}=2\pi r_{ea}L$, $A_{C/C}=2\pi r_{in}L$, and $A_{C/E}=2\pi r_{ec}L$.

When the cell voltage (V_{cell}) is provided, the electronic potentials at E/C interfaces are set and the ionic potentials at E/E interfaces satisfy the continuous condition

$$\begin{aligned} &x_i|_{E/C}=x_{i,b},\ N_i|_{E/E}=0,\quad \phi_{el}|_{A/C}=0,\ \phi_{el}|_{C/C}=V_{cell},\quad \left.\frac{d\phi_{el}}{dz}\right|_{E/E}=0\\ &\left.\frac{d\phi_{ion}}{dz}\right|_{E/C}=0,\quad \sigma_{ion,a}^{eff}\left.\frac{d\phi_{ion}}{dz}\right|_{A/E}^{-}=\sigma_{ion}\left.\frac{d\phi_{ion}}{dz}\right|_{A/E}^{+},\ \sigma_{ion}\left.\frac{d\phi_{ion}}{dz}\right|_{C/E}^{-}=\sigma_{ion,c}^{eff}\left.\frac{d\phi_{ion}}{dz}\right|_{C/E}^{+} \end{aligned} \tag{20}$$

Thus, the total overpotential (η_t) of the electrode can be obtained from the overpotential distribution. For PSOFC,

$$\eta_{t,k}=\frac{1}{\sigma_{el,k}^{eff}+\sigma_{ion,k}^{eff}}\left[\sigma_{ion,k}^{eff}\eta_k|_{E/C}+\sigma_{el,k}^{eff}\eta_k|_{E/E}+\frac{\psi J}{A_{E/E}}\delta_k\right]\quad (k=a,c) \tag{21}$$

For TSOFC,

$$\eta_{t,k}=\frac{1}{\sigma_{el,k}^{eff}+\sigma_{ion,k}^{eff}}\left[\sigma_{ion,k}^{eff}\eta_k|_{E/C}+\sigma_{el,k}^{eff}\eta_k|_{E/E}+\frac{\psi J}{2\pi L}\ln\frac{r_{k,out}}{r_{k,in}}\right]\quad (k=a,c) \tag{22}$$

4.1.2. Interface-type PEN model

Most electrochemical and chemical reactions occur in the thin zones which are close to the two sides of the electrode. So in the interface (INT-) type PEN model, it is assumed that electrochemical reactions only occur at the electrode/electrolyte interface, and reforming and WGS chemical reactions only occur at the anode/flow channel interface. This simplification has been widely used in cell-level and system-level analysis.

In this research the mass balance of species is directly related to the electrochemical flux

$$\nabla\cdot(x^m N_i)=0,\quad N_i|_{E/E}=-\sum_{k=H_2,CO\text{ or }O_2}\frac{\psi\upsilon_{i,k,elec}J_k}{(n_eFA_{E/E})} \tag{23}$$

With the given bulk concentration at the E/C interface, $x_i|_{E/C}=x_{i,b}$, the species molar fraction can be obtained by integrating Eq. (16).

For the methane-fueled system, there is both H_2 and CO electrochemical oxidation. The ratio of H_2 electrochemical current to the total current as $\omega=J_{H_2}/J$ was defined using the equations: $J_{H_2}+J_{CO}=J_{O_2}=J$, $J_{H_2}=\omega J$, and $J_{CO}=(1-\omega)J$. If CO oxidation is neglected, $\omega=1$. Assuming the same total overpotential in H_2 and CO electrochemical reactions (η_t), the general current–overpotential relationship is

$$\frac{J_k}{A_{E/E}}=I_{0,k}\left[\frac{c_{react,TPB}}{c_{react,b}}\exp\left(\frac{\alpha n_eF}{\Re T}\psi\eta_t\right)-\frac{c_{prod,TPB}}{c_{prod,b}}\exp\left(-\frac{\beta n_eF}{\Re T}\psi\eta_t\right)\right] \tag{24}$$

where I_{0,H_2} and $I_{0,CO}$ are the exchange current density of H_2 and CO based on the active area at the E/E interface (A_{EE}), which are related to the temperature and species concentrations shown in Eq. (15). Without considering the variation of gas concentrations ($c_{i,TPB}=c_{i,b}$), Nagata et al. [15] and Iwata et al. [16] presented different modified Butler–Volmer type relationships between the exchange current density and the activation polarization.

Generally for the INT-type PEN model, the operating current is provided to obtain the cell voltage. In order to obtain the explicit expression of the total overpotential (i.e. $\eta_t=f(J)$) instead of the implicit calculation in Eq. (24), the activation polarization and the concentration polarization are usually calculated separately. From the Butler–Volmer equation, the linear expression of exponent items or the well-known Tafel equation is often used at a small or high activation polarization, respectively [17]. For simplicity, the semi-empirical expressions of the activation resistance (R_{act}) in Arrhenius's form are also widely used [18].

$$\frac{1}{R_{act,k}}=-\frac{n_eF}{\upsilon_{k,elec}\Re T}k_k\left(\frac{p_k}{p_0}\right)^n\exp\left(-\frac{E}{\Re T}\right)\qquad (k=H_2,\text{CO or }O_2) \tag{25}$$

where $\upsilon_{H_2,elec}=\upsilon_{CO,elec}=-1$, $\upsilon_{O_2,elec}=-0.5$, k is the pre-exponent factor, and the power index n is for pressure correction. When considering the parallel connection between the H_2 and CO activation resistances (i.e. $J_{H_2}R_{act,H_2}=J_{CO}R_{act,CO}$), the activation polarization (η_{act}) can be obtained by

$$\eta_{act,a}=\frac{\psi J}{(A_{A/E}/R_{act,H_2})+(A_{A/E}/R_{act,CO})},\quad \eta_{act,c}=\frac{\psi JR_{act,O_2}}{A_{C/E}} \tag{26}$$

The concentration polarization (η_{conc}) is the degradation of the electromotive force associated with the species concentration variation from $c_{i,b}$ to $c_{i,TPB}$. Thus the total overpotential of the electrode can be obtained by $\eta_{t,k}=\eta_{act,k}+\eta_{conc,k}$. The calculation of the electromotive force (or the open circuit voltage) of the fuel mixture is introduced in the next section.

4.1.3. Open circuit voltage of multi-component fuel

The open circuit voltage (V_{oc}) is the cell voltage when there is no current flow. The open circuit voltage for the multi-component fuel can be related to the Gibbs free energy variation in the direct oxidation reaction of the fuel mixture. For the methane-fueled system, $x_{H_2}[H_2]+x_{CO}[CO]+x_{CH_4}[CH_4]+(0.5x_{H_2}+0.5x_{CO}+2x_{CH_4})[O_2]\rightarrow(x_{CO}+x_{CH_4})[CO_2]+(x_{H_2}+2x_{CH_4})[H_2O]$, the total electron transfer number of direct electrochemical oxidation of H_2, CO, and CH_4, is $n_{e,mix}=2x_{H_2}+2x_{CO}+8x_{CH_4}$. So the open circuit voltage can be obtained by

$$\begin{aligned} V_{OC}=\frac{1}{2(x_{H_2}+x_{CO}+4x_{CH_4})F}\Big\{&-(x_{H_2}\Delta G_{H_2,ox}+x_{CO}\Delta G_{CO,ox}\\ &+x_{CH_4}\Delta G_{CH_4,ox})_{p=p_0}+\Re T[x_{H_2}\ln p_{H_2}+x_{CO}\ln p_{CO}\\ &+x_{CH_4}\ln p_{CH_4}-(x_{CO}+x_{CH_4})\ln p_{CO_2}-(x_{H_2}+2x_{CH_4})\ln p_{H_2O}\\ &+(0.5x_{H_2}+0.5x_{CO}+2x_{CH_4})\ln p_{O_2}]\Big\} \end{aligned} \tag{27}$$

where $\Delta G_{ox,p_0}$ and $\Delta S_{ox,p_0}$ are the variation of Gibbs free energy and entropy of H_2, CO and CH_4 oxidation reactions at standard pressure, respectively. For the binary system of H_2–H_2O or CO–CO_2, the above equation is identical to the well-known Nernst equation. With the reference values of ΔG_{ref} and ΔS_{ref}, ΔG is generally calculated by $(\Delta G)_p=(\Delta G_{ref})_p-\Delta S_{ref}(T-T_{ref})$. However, its accuracy is strongly dependent on the choice of the reference temperature, T_{ref}. From the relationship between the specific heat of ideal gas and temperature $C_p=f(T)$ in the gPROMS database, the species Gibbs

free energy can be calculated without choosing the reference temperature, as described in detail in Appendix A. This calculation is suitable for different types of fuel cells in a wide range of working temperatures.

In the case of zero current flow, there is no diffusion process and the concentration of each species is equal to its bulk concentration, i.e. $V_{oc} = f(x_{i,b})$. A lower Nernst potential, $V_{oc,TPB} = f(x_{i,TPB})$, can be obtained when substituting $c_{i,TPB}$ for $c_{i,b}$ in Eq. (27). Then, the concentration polarization is calculated by $\eta_{conc} = \psi(V_{oc} - V_{oc,TPB})$.

4.1.4. Ohmic polarization

Assuming that the current is almost perpendicularly collected, meaning the current flows normally through the tri-layer of PEN, the ohmic polarization (η_{ohm}) of PSOFC can be easily calculated by

$$\eta_{ohm} = \eta_{ohm,a} + \eta_{ohm,e} + \eta_{ohm,c} = \frac{J}{A_{E/E}} \sum_{k=a,c,e} \frac{\delta_k}{\sigma_{k,eff}} \tag{28}$$

where $\sigma_{eff} = \sigma_{ion,eff} + \sigma_{el,eff}$ is the effective conductivity of the individual layer. Notice that the charge transfer in the two phases (Eq. (14)) has been considered in the CV-type PEN model, which means the ohmic polarization of electrodes is included in the total overpotential (Eq. (21) or Eq. (22)). Therefore, only the ohmic polarization of the electrolyte layer, $\eta_{ohm,e}$ need be considered in the CV-type PEN model.

Due to the existence of the current pathway in both the radial and the circumferential direction in TSOFC, the calculation of the ohmic polarization in TSOFC is much more complex than in PSOFC. Generally, a multi-dimensional model or a network circuit model of current flow is required for accurate calculation [19]. To avoid the presence of the radial and circumferential coordinates in an axial distributed tubular cell model, a so-called transmission-line analytical model has been used to calculate the resistivity, R_{ohm} (Ω m) [11]:

$$R_{ohm} = \frac{R_1}{R_2} + \frac{\sqrt{\sigma_c \delta_{ic}/\sigma_{ic}\delta_c}}{2\tanh(J_{ic})}, \quad J_{ic} = \frac{L_{ic}}{2}\sqrt{\frac{\sigma_{ic}}{\sigma_c \delta_{ic}}\frac{1}{\delta_c}}$$

$$R_1 = \left[\left(\frac{1}{\sigma_a \delta_a}\right)^2 + \left(\frac{1}{\sigma_c \delta_c}\right)^2\right]\cosh(J_e) + \frac{2 + J_e \sinh(J_e)}{\sigma_a \delta_a \sigma_c \delta_c} \tag{29}$$

$$R_2 = 2\left(\frac{\sigma_e}{\delta_e}\right)^{1/2}\left(\frac{1}{\sigma_a \delta_a} + \frac{1}{\sigma_c \delta_c}\right)^{3/2}\sinh(J_e), \quad J_e = \frac{L_e}{2}\sqrt{\frac{\sigma_e}{\delta_e}\left(\frac{1}{\sigma_a \delta_a} + \frac{1}{\sigma_c \delta_c}\right)}$$

where δ_{ic} is the interconnector thickness, and $L_e = \pi(r_{ea} + r_{ec})$ and L_{ic} are the circumference of electrolyte layer and the interconnector, respectively. Thus, the ohmic polarization of TSOFC can be obtained by $\eta_{ohm} = 2\pi I R_{ohm} r_{out}$. For a lumped calculation, the current density $I = J/(2\pi r_{out} L)$, i.e. $\eta_{ohm} = J R_{ohm}/L$.

For both PSOFC and TSOFC, the cell voltage can be calculated by $V_{cell} = V_{oc} - \eta_{t,a} - |\eta_{t,c}| - \eta_{ohm} - \eta_{leak}$, where η_{leak} is the polarization for leakage loss.

4.1.5. Advanced PEN model

During the cases of low and medium electric loading or low reactant utilization, the above-mentioned CV-type and INT-type PEN models were validated by the button cells' experimental data. However, there was an obvious discrepancy in the general PEN models when the current density or fuel utilization is high.

The overestimation of the general PEN model during critical conditions was mainly attributed to ignoring details of heterogeneous reaction mechanisms, such as surface diffusion and absorption/desorption processes. An advanced PEN model based on the diffusion equivalent circuit was developed in our SOFC model library to avoid the complex kinetic analysis of elementary steps, which is not suitable for direct use in high-level modeling [20].

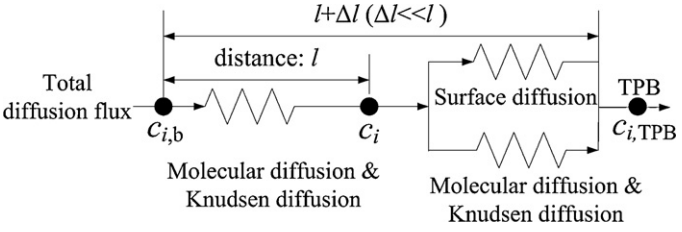

Fig. 5. Diffusion equivalent circuit for correction of the species concentration at TPB.

As shown in Fig. 5, the resistance of surface diffusion was assumed to follow the gaseous molecular diffusion. Two steps of mass transfer were assumed [21]: (1) via bulk diffusion, the species concentration varied from the bulk concentration $c_{i,b}$ to the local intrinsic concentration at the site adjacent to TPB c_i (or only the concentration at TPB, $c_{i,TPB}$ for the general PEN models, as shown in Eq. (15)). (2) via surface diffusion, it reached the real concentration at TPB, $c_{i,TPB}$. The diffusion distance of the two steps were l and Δl, respectively (with $l \gg \Delta l$ generally).

According to the theory of Langmuir isothermal absorption, the surface coverage of species i at the Ni surface of the anode, θ_i is

$$\theta_i = \frac{b_i p_i}{1 + \sum_i b_i p_i}, \quad b_i = \frac{N_A \pi r_i^2 \tau_0}{\sqrt{2\pi \Re T M_i}} \exp\left(\frac{Q_i}{\Re T}\right) \tag{30}$$

where b_i is the Langmuir parameter, N_A is Avogadro's number, r_i and M_i are the molecular radius and molecular weight of species i, respectively, τ_0 is the vibrational period (10^{-13} s), and Q_i is the activation energy for adsorption. In general, the value of θ_i is small at the high operating temperature of SOFC. The relative surface coverage of species i, $\Theta_i = \theta_i / \Sigma_i \theta_i$, is used instead of the absolute coverage.

According to the serial diffusion equivalent circuit and first Fick's law, the species concentration at TPB can be corrected by

$$c_{i,TPB} = c_{i,b} - \left(\frac{D_i}{D_{s,i}}\right)^{1-\Theta_i}(c_{i,b} - c_i) \tag{31}$$

The above equation should only be used for the concentration correction of reactant species (H_2, CO). The product and inert species (H_2O, CO_2, N_2) only influence the relative coverage via competitive absorption, as shown in Eq. (30). The bulk diffusivity D_i, and the surface diffusion coefficient $D_{s,i}$, can be described as

$$D_i = \frac{1 - x_i}{\sum_{j \neq i}(x_j / D_{ij})}, \quad D_{s,i} = \frac{D_{s,i,0}^{1-\Theta_i} D_{s,i,1}^{\Theta_i}}{1 - \Theta_i} \tag{32}$$

where $D_{s,i,0}$ and $D_{s,i,1}$ are the surface diffusion coefficients at zero coverage ($\Theta_i \approx 0$) or full coverage ($\Theta_i \approx 1$), respectively [22]. In general, $D_{s,i,0} \gg D_{s,i,1}$.

When substituting Eq. (31) into the general current–overpotential equation, Eq. (15), the advanced PEN model is formed, keeping the same structure and boundary conditions as the general PEN models. Because the overall resistance of mass transfer was considered, the advanced PEN model improved the predicted accuracy over a wide range and has been validated

in the cases of different fuel components for the H_2–H_2O, CO–CO_2, H_2–CO, and H_2–CO_2 fuel system [20].

4.1.6. Approximate analytical PEN model

Compared to semi-empirical calculations, the above mathematical models provided a more detailed and accurate simulation but at a higher numerical cost. However, for some applications, such as the model-based hardware-in-the-loop simulation or simplification of multi-dimensional numeration, a balance between the mechanistic and empirical models is often required for both accurate and fast computations.

Usually, the dominant variables of the species concentration and overpotential are strongly coupled in the nonlinear system of PEN-level models. Thus, an exact analytical solution is difficult to obtain. For the binary fuel system (e.g. H_2–H_2O, CO–CO_2), an approximate analytical solution of the general CV-type PEN model was developed based on the perturbation method. For a thick electrode, such as the anode in an anode-supported SOFC, the explicit expression of the overpotential distribution could be obtained using the singular perturbation method, which consisted of a logarithmic item and two exponential items [23]

$$\eta(\tilde{x}) = \frac{\Re T}{n_e F(\alpha+\beta)} \ln^{[1-x_{1,b}(1-b\tilde{x})]/[(1-x_{1,b})(1-b\tilde{x})]} + \varepsilon C_6 e^{-\lambda_1(1-\tilde{x})/\varepsilon} + \varepsilon C_8 e^{-\lambda_2\tilde{x}/\varepsilon} \quad (33)$$

where $\tilde{x} = x/\delta$ is the dimensionless electrode thickness, $x_{1,b}$ is the fuel (H_2 or CO) molar fraction, and the small perturbation variable ($\varepsilon \approx 0$) and the constants (λ_1, λ_2, C_6, C_8) are related to the operational conditions and electrode property [23].

For an electrode with a small thickness, the approximate analytical solution of the PEN model can be obtained using the regular perturbation method [23]. The analytical distribution of overpotential has also been obtained by neglecting the variation of gas concentration [24]. However, the linear expansion of the exponential term was only accurate enough at a low overpotential. For PSOFC, there was a system of $d^2\eta/d^2x = f(\eta)$, which had the exact implicit solution $(d\eta/dx)^2 = \int 2f(\eta)d\eta + const$. Considering $\sigma_{ion} \ll \sigma_{el}$, the overpotential at the E/C interface is generally negligible, i.e. $\eta|_{E/C} \approx 0$. With the boundary conditions of $(d\eta/dx)|_{E/E}$ and $(d\eta/dx)|_{E/C}$ in Eq. (19), the overpotential at the E/E interface was obtained without solving the distribution

$$\frac{1}{\alpha}e^{\alpha f\psi\eta|_{E/E}} + \frac{1}{\beta}e^{-\beta f\psi\eta|_{E/E}} = \frac{\sigma_{eff} f}{2 i_0 S_{TPB}}\left[\left(\frac{J}{A_{E/E}\sigma_{ion}^{eff}}\right)^2 - \left(\frac{J}{A_{E/C}\sigma_{el}^{eff}}\right)^2\right] + \left(\frac{1}{\alpha}+\frac{1}{\beta}\right) \quad (34)$$

where $f = n_e F/\Re T$ and $1/\sigma_{eff} = 1/\sigma_{ion,eff} + 1/\sigma_{el,eff}$. There was an explicit solution when $\alpha = \beta$. The total overpotential could be further obtained from Eq. (21). Considering the diluting influence of N_2 and low O_2 utilization for cell cooling, the variation of O_2 concentrations in the cathode was usually small. This method can also be used to calculate the total cathodic overpotential in the cathode-supported planar SOFCs.

4.2. Quasi-equilibrium cell-level model

The gaseous species mass balance in the anode (k = a) and the cathode (k = c) is

$$\dot{n}_{k,in}x_{i,k,in} + A_{E/C}\left[-\psi N_{i,k}\big|_{E/C} + (\upsilon_{i,ref}R_{ref} + \upsilon_{i,WGS}R_{WGS})\right] = x_{i,k}\sum_i \times \left(\dot{n}_{k,in}x_{i,k,in} + A_{E/C}\left[-\psi N_{i,k}\big|_{E/C} + (\upsilon_{i,ref}R_{ref} + \upsilon_{i,WGS}R_{WGS})\right]\right) = x_{i,k}\dot{n}_{k,out} \quad (35)$$

where $\dot{n}_{in}$ and $\dot{n}_{out}$ are the inlet and outlet molar flow rate, respectively, $x_{i,in}$ and x_i are the inlet and outlet species molar fraction, respectively, and $N_i|_{E/C}$ is the species flux at the E/C interface from the PEN model. Note that only the INT-type PEN model was used in the quasi-equilibrium cell-level model.

Assuming that the gaseous components at the fuel outlet were in thermodynamic equilibrium, the chemical reaction rate in the anode, R_{ref} and R_{WGS} can be obtained by

$$K_{eq,ref}x_{CH_4}x_{H_2O} = \left(\frac{p_a}{p_0}\right)^2 x_{H_2}x_{CO}, \quad K_{eq,WGS}x_{CO}x_{H_2O} = x_{H_2}x_{CO_2} \quad (36)$$

In the cathode, $R_{ref} = R_{shift} = 0$. Assuming the outlet gas temperature is the same as the cell operating temperature, there is the energy balance

$$\dot{n}_{a,in}H_{a,in} + \dot{n}_{c,in}H_{c,in} = \dot{n}_{a,out}H_{a,out} + \dot{n}_{c,out}H_{c,out} + JV_{cell} + Q_{loss} \quad (37)$$

where Q_{loss} is the heat loss, and H is the gas molar specific enthalpy. For ideal gases,

$$H = \sum_i x_i H_i \quad H_i(T) = H_i(T_0) + \int_{T_0}^{T} C_{p,i}(t)\,dt \quad (38)$$

where $C_{p,i}$ is the molar specific heat of species i.

4.3. Lumped cell-level model

In the lumped cell model, flow channels are considered as continuous stirred reactors (CSTR), i.e. the gas thermodynamic state at the outlet is the same in the flow channel. When considering the volume dynamics of flow filling and emptying, the species and total mass balance in the flow channels are

$$V_k c_{t,k}\frac{dx_{i,k}}{dt} = \dot{n}_{k,in}(x_{i,k,in} - x_{i,k}) + \psi_{INT}A_{E/C}(R_i - x_{i,k}\sum_i R_i) - \psi A_{E/C}\left(N_{i,k}\big|_{E/C} - x_{i,k}\sum_i N_{i,k}\big|_{E/C}\right) \quad (39)$$

$$V_k\frac{dc_{t,k}}{dt} = \dot{n}_{k,in} - \dot{n}_{k,out} - A_{E/C}\sum_i\left(\psi N_{i,k}\big|_{E/C} - \psi_{INT}R_i\right) \quad (k = a, c) \quad (40)$$

where $c_{t,k}$ is the total gas concentration in the flow channel, $R_i = \upsilon_{i,ref}R_{ref} + \upsilon_{i,shift}R_{WGS}$ is the total chemical reaction rate per unit area at the E/C interface, and ψ_{INT} represents the type of PEN model. For the INT-type PEN model (with $\psi_{INT} = 1$), the chemical reactions appear at the E/C interface, and the species flux $N_{i,k}|_{E/C}$ only reflects the electrochemical flux. For the CV-type PEN model, $\psi_{INT} = 0$, $N_{i,k}|_{EC}$ includes both the electrochemical and chemical flux.

In the cathode, $R_{ref} = R_{shift} = 0$. The kinetics of the methane reforming reaction based on the apparent area of the A/C interface, R_{ref} (mol m^{-2} s^{-1}) is [25]

$$R_{ref} = 4274\frac{p_a}{p_0}\exp\left(-\frac{82,000}{\Re T}\right)\left(x_{CH_4} - \frac{p_a^2}{p_0^2}\frac{x_{CO}x_{H_2}^3}{K_{eq,ref}x_{H_2O}}\right) \quad (41)$$

In general, the water gas shift reaction can be thought to be in equilibrium at any time. To avoid the hybrid system of algebraic expression (Eq. (36)) and differential equations, the unified kinetic expression for the WGS reaction is [10]

$$R_{WGS} = k_{WGS}\left(\frac{x_{CO}x_{H_2O} - x_{CO_2}x_{H_2}}{K_{eq,WGS}}\right) \quad (42)$$

where the kinetic constant k_{WGS} is an arbitrarily large value limited by numerical stability.

Similar to the quasi-equilibrium model, the gas temperatures and the solid temperature are assumed to be equal to the cell operating temperature. Thus, the energy balance is

$$\rho_s c_{p,s} V_s \frac{dT}{dt} = \sum_{k=a,c} \dot{n}_{k,in} H_{k,in} - \sum_{k=a,c} \dot{n}_{k,out} H_{k,out} - JV_{cell} - Q_{loss} \quad (43)$$

When considering the heat capacity of the gas phase being much less than that of the solid phase, only the temperature dynamics of the solid phase was considered for simplicity.

Generally, the initial condition of the lumped cell model was set as the given temperature, total gas pressure, and $n-1$ species concentrations. And the total outlet gas flow rate, $\dot{n}_{out}$ was related to the pressure difference between the gas pressure and the downstream pressure. Therefore, the flow-resistance performance of downstream valves or pipes also influences the volume dynamics.

4.4. Distributed cell-level model

Due to its high operating temperature, the temperature distribution and local hotspot in SOFC are important for its healthy operation. Only the dominant axial temperature distribution along the direction of cell length was considered in our distributed cell model, where concurrent and countercurrent flow modes can be analyzed.

4.4.1. Gas pressure drop

For simplicity, the pressure distribution was not considered here. The total gas pressure drop in the anode and cathode flow channel was

$$\Delta p_k = p_{k,in} - p_{k,out} = 0.5\rho_{k,in} u_{k,in}^2 \left[\frac{c_{f,k} L}{(Re_k D_{e,k})} + \zeta_{k,in} + \zeta_{k,out} \right] \quad (44)$$

where ρ_{in} and u_{in} are the inlet gas density and velocity, respectively, c_f is the Colburn friction factor, ζ_{in} and ζ_{out} are the inlet and outlet friction coefficient, respectively, and the Reynold number Re is an approximate calculation from the inlet gas property (i.e. $Re = \rho_{in} u_{in} D_e / \mu_{in}$, where μ_{in} is the inlet gas dynamic viscosity).

Similarly, the pressure drop of the preheated air in the air supply tube of TSOFC is

$$\Delta p_{air} = p_{air,in} - p_{air,out} = 0.5\rho_{air,in} u_{air,in}^2 \left[\frac{c_{f,AST} L}{2Re_{air} r_{AST,in}} + \zeta_{AST,in} + \zeta_{AST,out} \right] \quad (45)$$

where $Re_{air} = 2\rho_{air,in} u_{air,in} r_{AST,in} / \mu_{air,in}$, and the gas pressure at the inlet of the cathode flow channel is equal to the outlet of the air supply tube (i.e. $p_{c,in} = p_{air,out}$).

The total gas pressure in each part was obtained using the average of the inlet and outlet pressure (i.e. $p_k = 0.5(p_{k,in} + p_{k,out})$).

4.4.2. Gas phase mass and energy balance

Along the axial coordinate $z \in [0, L]$, the species mass balance in flow channels was

$$c_{t,k} \frac{\partial x_{i,k}}{\partial t} = -c_{t,k} u_k \frac{\partial x_{i,k}}{\partial z} - S_{k,PEN} \zeta_{rib} \psi \left(N_{i,k}|_{E/C} - x_{i,k} \sum_i N_{i,k}|_{E/C} \right) + \psi_{INT} S_{k,PEN} \left(R_i - x_{i,k} \sum_i R_i \right) \quad (k = a, c) \quad (46)$$

where u is the gas velocity and S_{PEN} is shown in Eq. (8) or (9). The chemical reaction rate in the anode is shown in Eqs. (41) and (42), which is only effective for the INT-type PEN model ($\psi_{INT} = 1$).

The energy balance of gas phase in the anode and the cathode is

$$c_{t,k} C_{p,k} \frac{\partial T_k}{\partial t} = -c_{t,k} u_k C_{p,k} \frac{\partial T_k}{\partial z} + Q_k \quad (k = a, c) \quad (47)$$

where T_a and T_c are the gas temperatures in the anode and cathode, and $C_{p,k} = \Sigma_i C_{p,i} x_{i,k}$ is the gas molar specific heat. In the anode, the heat source item, Q_a is

$$Q_a = S_{a,PEN} \left[h_{a,PEN}(T_{PEN} - T_a) - \psi_{INT} \sum_i (\upsilon_{i,ref} H_{i,a} R_{ref} + \upsilon_{i,WGS} H_{i,a} R_{WGS}) + \sum_i 0.5\zeta_{rib} (|N_{i,a}|_{A/C}| - N_{i,a}|_{A/C}) C_{p,i} (T_{PEN} - T_a) \right] + \psi_P S_{a,CON} h_{a,CON} (T_{CON} - T_a) \quad (48)$$

The first item on the right side of the above equation represents the convection heat exchange between fuel and the PEN, where T_{PEN} is the PEN temperature and $h_{a,PEN}$ is the corresponding convective heat transfer coefficient. The second item is the chemical reaction heat of the reforming and shift reaction at the anode/flow channel interface, which is only effective for the INT-type PEN model. The third item represents the variation of the species enthalpy due to mass transfer. It brings sensible heat flow related to temperature difference when the species is transported from the PEN to the anode flow channel, i.e. $N_{i,a}|_{A/C} < 0$. The fourth item represents the convective heat exchange between the fuel and the interconnector of PSOFC, where T_{CON} is the interconnector temperature, $h_{a,CON}$ is the corresponding convective heat transfer coefficient, $\psi_P = 1$ indicates being solely effective for PSOFC, and $\psi_P = 0$ for TSOFC.

Similarly, the heat source item, Q_c in the cathode is

$$Q_c = S_{c,PEN} h_{c,PEN} (T_{PEN} - T_c) + \psi_P S_{c,CON} h_{c,CON} (T_{CON} - T_c) + (1 - \psi_P) S_{AST} h_{c,AST} (T_{AST} - T_c) \quad (49)$$

where $h_{c,PEN}$, $h_{c,CON}$ and $h_{c,AST}$ are the convective heat transfer coefficients between the gas and the PEN, the interconnector of PSOFC and the air supply tube of TSOFC, respectively. T_{AST} is the temperature of the air supply tube.

In principle, the dynamics of the total gas concentration, $\partial c_t / \partial t$, can be obtained from the sum of the species mass balance (Eq. (46)). However, by neglecting the dynamics of the total gas pressure, $\partial p / \partial t = 0$, the joint calculation of $\partial c_t / \partial t$ and $\partial T / \partial t$ contradicts the ideal gas law, $p = c_t \Re T$, and creates difficulty in setting the initial condition. In some literature [10,11], the constant gas velocity was assumed to avoid the numerical calculation problem. Nevertheless, the variation of gas velocity should not be neglected because of the significant variation of gas temperature and the small variation of total pressure in the flow channels.

Considering $\partial c_t / \partial t = \partial (p / \Re T) / \partial t = -(c_t / T)\ \partial T / \partial t$, the total gas mass balance can be described as the following ordinary differential equation [8]

$$0 = -\frac{\partial (c_{t,k} u_k T_k)}{\partial z} - T_k S_{k,PEN} \left(\zeta_{rib} \psi \sum_i N_{i,k}|_{E/C} - \psi_{INT} \sum_i R_i \right) + \frac{Q_k}{C_{p,k}} \quad (50)$$

Similarly, the gaseous mass and energy balance in the air supply tube of TSOFC is

$$0 = -\frac{\partial (c_{t,air} u_{air} T_{air})}{\partial z} + \frac{1}{C_{p,air}} \frac{2}{r_{AST,in}} h_{air,AST} (T_{AST} - T_{air}) \quad (51)$$

$$c_{t,air}C_{p,air}\frac{\partial T_{air}}{\partial t} = -c_{t,air}u_{air}C_{p,air}\frac{\partial T_{air}}{\partial z} + \frac{2}{r_{AST,in}}h_{air,AST}(T_{AST} - T_{air}) \quad (52)$$

where $h_{air,AST}$ is the convective heat transfer coefficient between the preheated air and AST (there is no variation of species concentration in AST).

4.4.3. Solid-phase energy balance

The energy conversation of PEN is

$$\begin{aligned}\rho_{PEN}c_{p,PEN}\frac{\partial T_{PEN}}{\partial t} &= \kappa_{PEN}\frac{\partial^2 T_{PEN}}{\partial z^2} - S_{m,PEN,c}\sum_i N_{i,c}|_{C/C}H_{c,i}(T_c) \\ &+ \frac{S_{m,PEN,a}}{2}\sum_i[(N_{i,a}|_{A/C} + |N_{i,a}|_{A/C}|)H_{a,i}(T_a) \\ &+ (N_{i,a}|_{A/C} - |N_{i,a}|_{A/C}|)H_{a,i}(T_{PEN})] \\ &- S_{m,PEN,c}I(z)V_{cell} \\ &+ \sum_{k=a,c}S_{h,PEN,k}h_{k,PEN}(T_k - T_{PEN}) \\ &- \sum_{k=a,c}S_{h,PEN,k}q_{PEN,k}\end{aligned} \quad (53)$$

The first item on the right side of the above equation is heat conduction. The second and third items represent the variation of gas enthalpy because of the species mass transfer between the flow channel and the PEN. Here, the temperature of the species which flows into the PEN is the gas phase temperature, and the temperature of the species which flows out of the PEN is the PEN temperature. The summation of these two items is the total electrochemical and chemical reaction heat. The fourth item is the electric power, where $I(z)$ is the local current density. The fifth item is the convection heat transfer between the gas phase and the PEN, and the sixth item is the radiation heat transfer. For gray bodies, the radiation heat flux out of the PEN element surface, q_{PEN} is related to the corresponding radiosity or net loss of radiation heat flux, B_{PEN}

$$q_{PEN,k}(z) = \frac{\in_{PEN}\left[\sigma_B T_{PEN}^4(z) - B_{PEN}(z)\right]}{(1 - \in_{PEN})} \quad (k = a, c) \quad (54)$$

where $\in_{PEN}$ is the emissivity of the PEN and σ_B is the Boltzmann constant.

For the radiation systems of PSOFC and TSOFC, the radiosity of the PEN surface and the temperature distribution are strongly dependent on the system configuration

$$\begin{aligned}B_{PEN,k}(z) = {} & \in_{PEN}\sigma_B T_{PEN}^4(z) + (1 - \in_{PEN})\sigma_B T_e^4 F_{dPENz,end,k} \\ & + (1 - \in_{PEN})\left[\int_0^L B_{PEN}(x)\,dF_{dPENz,dPENx,k}\right. \\ & + \psi_P\int_0^L B_{CON,k}(x)\,dF_{dPENz,dCONx,k} \\ & \left. + (1 - \psi_P)\int_0^L B_{AST,out}(x)\,dF_{dPENz,dASTx,out,k}\right] \\ & \times (k = a, c)\end{aligned} \quad (55)$$

where B_{CON} and $B_{AST,out}$ are the radiosity of the CON and outer AST infinitesimal element surface, respectively, T_e is the effective blackbody temperature of the environment, which is usually set to be the gas temperature at the inlet or outlet flow channel [26], $F_{dPEN,end}$ is the finite view factor between the PEN element and environment, and $dF_{dPEN,dPEN}$, $dF_{dPEN,dCON}$, and $dF_{dPEN,dAST}$ are the differential view factors between the PEN element and the PEN, CON, and AST elements, respectively,as described in detail in Appendices B and C.

The energy balance of the interconnector in PSOFC and the air supply tube in TSOFC can be similarly obtained by

$$\begin{aligned}&\rho_{CON}c_{p,CON}\frac{\partial T_{CON}}{\partial t} \\ &= \kappa_{CON}\frac{\partial^2 T_{CON}}{\partial z^2} + \frac{1}{A_{CON}}\sum_{k=a,c}(W_{ch} + 2D_k) \\ &\times \left[h_{k,CON}(T_k - T_{CON}) - \frac{\in_{CON}}{1 - \in_{CON}}(\sigma_B T_{CON}^4 - B_{CON,k})\right]\end{aligned} \quad (56)$$

$$\begin{aligned}&\rho_{AST}c_{p,AST}\frac{\partial T_{AST}}{\partial t} \\ &= \kappa_{AST}\frac{\partial^2 T_{AST}}{\partial z^2} + \frac{2}{r_{AST,out}^2 - r_{AST,in}^2} \\ &\times \left[r_{AST,out}h_{c,AST}(T_c - T_{AST}) + r_{AST,in}h_{air,AST}(T_{air} - T_{AST})\right. \\ &- r_{AST,out}\in_{AST}\left(\frac{\left(\sigma_B T_{AST}^4 - B_{AST,out}\right)}{(1 - \in_{AST})}\right) - r_{AST,in}\in_{AST} \\ &\left.\times\left(\frac{\left(\sigma_B T_{AST}^4 - B_{AST,in}\right)}{(1 - \in_{AST})}\right)\right]\end{aligned} \quad (57)$$

where $\in_{CON}$ and $\in_{AST}$ are the emissivity of the interconnector and air supply tube, respectively, and the corresponding radiosity of the element surface, B_{CON}, $B_{AST,out}$ and $B_{AST,in}$ are obtained by

$$\begin{aligned}B_{CON,k}(z) = {} & \in_{CON}\sigma_B T_{CON}^4(z) + (1 - \in_{CON})\left[\sigma_B T_e^4 F_{dCONz,end,k}\right. \\ & + \int_0^L B_{CON,k}(x)\,dF_{dCONz,dCONx,k} \\ & \left. + \int_0^L B_{PEN,k}(x)\,dF_{dCONz,dPENx,k}\right] \quad (k = a, c)\end{aligned} \quad (58)$$

$$\begin{aligned}B_{AST,k}(z) = {} & \in_{AST}\sigma_B T_{AST}^4(z) + (1 - \in_{AST})\left[\sigma_B T_e^4 F_{dASTz,end,k}\right. \\ & + \int_0^L B_{AST,k}(x)\,dF_{dASTz,dASTx,k} \\ & \left. + \int_0^L B_{PEN,c}(x)\,dF_{dASTz,dPENx,k}\right] \quad (k = in, out)\end{aligned} \quad (59)$$

The view factors in the above equations are described in Appendices B and C in detail.

4.4.4. Initial and boundary conditions

At the inlet of the flow channels, the dominant variables of the gas molar fraction, velocity, and temperature satisfy the first type of boundary conditions. At the cathode inlet of PSOFC, it is $x_{i,c}|_{z=0} = x_{i,c,in}$, $u_c|_{z=0} = u_{c,in}$, $T_c|_{z=0} = T_{c,in}$. At the inlet of AST or cathode in TSOFC, there are $u_{air}|_{z=0} = u_{air,in}$, $T_{air}|_{z=0} = T_{air,in}$ and $x_{i,c}|_{z=L} = x_{air,in}$, $T_c|_{z=L} = T_{air}|_{z=L}$, $u_c|_{z=L} = -r^2_{AST,in}/(r^2_{in} - r^2_{AST,out})u_{air}|_{z=L}$. At the anode inlet of PSOFC and TSOFC, there are $x_{i,a}|_{z=0} = x_{i,a,in}$, $u_a|_{z=0} = u_{a,in}$, $T_a|_{z=0} = T_{a,in}$ for concurrent flow and $x_{i,a}|_{z=L} = x_{i,a,in}$, $u_a|_{z=L} = -u_{a,in}$, $T_a|_{z=L} = T_{a,in}$ for countercurrent flow.

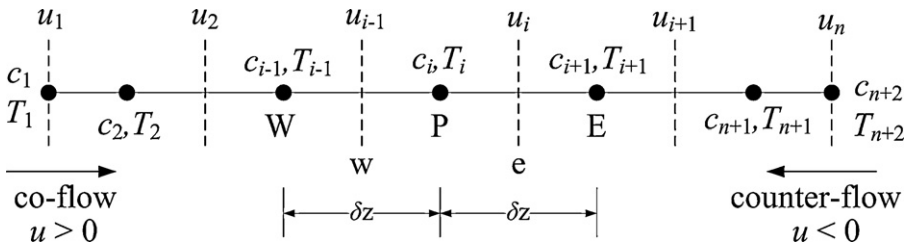

Fig. 6. Configuration of control volumes and stagger grids.

For simplicity, the adiabatic boundary conditions of solid phases are assumed, i.e. $\partial T_{PEN}/\partial z|_{z=0} = \partial T_{PEN}/\partial z|_{z=L} = 0$, $\partial T_{CON}/\partial z|_{z=0} = \partial T_{CON}/\partial z|_{z=L} = 0$ in PSOFC, and $\partial T_{AST}/\partial z|_{z=0} = \partial T_{AST}/\partial z|_{z=L} = 0$ in TSOFC. Because of the coupling solution of partial and ordinary differential equations, appropriate initial conditions including distribution of the gas concentration and temperature or velocity are necessary to improve the numerical performance.

4.4.5. Discrete method

gPROMS provides the finite difference method (FDM) and orthogonal collocation on finite elements method (OCFEM). It is a hybrid system of differential and integral equations due to the detailed radiant heat transfer in the above-distributed model. The discontinuity of the differential view factors of PSOFC (e.g. $f_1(X,Y) \to \infty$ as $Y = 0$ in Eq. (B1)) also brings numerical problems. If built-in discrete methods of gPROMS are used, a solution with a significant error of the overall heat balance or even an incorrect solution will be obtained. The control volume based discrete method and the stagger grids were used in this paper to solve this problem [27].

As shown in Fig. 6, the dominant variables of concentration and temperature are at the center of the control volume, while the gas velocity lies in the interface between control volumes. Because diffusion was not considered in the equation of gas mass balance (i.e. the Peclet number is infinite), the upwind scheme is considered a good method for interpolation at the velocity grid [27]. For the ith control volume, there are $cu(\partial x/\partial z) \approx c_{i-1}u_{i-1}(x_i - x_{i-1})/\delta z$, $\partial(cuT)/\partial z \approx (c_{i-1}u_{i-1}T_i - c_{i-1}u_{i-1}T_{i-1})/\delta z$ for concurrent flow, and $cu(\partial x/\partial z) \approx c_{i+1}u_i(x_{i+1} - x_i)/\delta z$ and $\partial(cuT)/\partial z \approx (c_{i+1}u_iT_{i+1} - c_iu_{i-1}T_i)/\delta z$ for countercurrent flow. The discretization is explained in detail in Appendix D. Combined with the discretization of the differential view factors, the relative error of the overall heat balance is reduced to less than 0.1%.

5. Calculation related to gas properties

The ideal physical properties foreign object (IPPFO) database in gPROMS generally satisfies most of the calculations of gas properties for the high-temperature SOFC application. Other calculations of physical properties, for example, the viscosity and conductivity of gas mixture, can be calculated more accurately from related literature [28].

In general, gas flow in the anode and cathode of SOFC is laminar. Assuming a developed flow, the convective heat transfer coefficient was calculated with the constant Nusselt number, Nu

$$h = \frac{Nu \cdot \kappa}{D_e} \tag{60}$$

where κ is the gas conductivity and D_e is the hydraulic diameter. The calculation of the Nusselt number of the fully developed laminar flow in the rectangular and circular channel with uniform wall temperature is easily available [29].

6. Performance parameters

The overall fuel utilization (U_f) and air stoichiometry (λ_{air}) is defined as

$$U_f = \frac{J}{[2F\dot{n}_{a,in}(4x_{CH_4,in} + x_{H_2,in} + x_{CO,in})]}, \quad \lambda_{air} = \frac{4F\dot{n}_{c,in}x_{O_2,in}}{J} \tag{61}$$

In the distributed model, the average current density (I_{avg}) and the average cell temperature ($T_{PEN,avg}$) can be calculated by

$$I_{avg} = \frac{1}{L}\int_0^L I(z)\,dz, \quad T_{PEN,avg} = \frac{1}{L}\int_0^L T_{PEN}(z)\,dz \tag{62}$$

For distributed calculation, the overall heat balance in PSOFC can be described as

$$\begin{aligned}\sum_{k=a,c}\dot{n}_{k,in}H_{k,in} &+ \int \sigma_B T_{e,k}^4 F_{dPEN,end,k}\,dA_{PEN,k} \\ &+ \int \sigma_B T_{e,k}^4 F_{dCON,end,k}\,dA_{CON,k} \\ = \sum_{k=a,c}\Bigg(&\dot{n}_{k,out}H_{k,out} + \int B_{PEN,k}F_{dPEN,end,k}\,dA_{PEN,k} \\ &+ \int B_{CON,k}F_{dCON,end,k}\,dA_{CON,k}\Bigg) + JV_{cell}\end{aligned} \tag{63}$$

The left side of the above equation represents the input heat of the system, Q_{in}, which includes the enthalpy of inflow gas and the radiant heat transfer from the environment. The right side of the above equation represents the output energy of the system, Q_{out}, which includes the enthalpy of outflow gas, the radiant heat transfer into the environment, and the electric power. The overall heat balance in TSOFC can be similarly obtained and is thus not listed due to limited space. The relative error of the overall heat balance is defined as $1 - Q_{in}/Q_{out}$.

7. Simulation and discussion

7.1. Test data for validation

In this paper, the multi-level SOFC models are validated by comparison with the experimental data of the IEA Benchmark Test [30]. Numerical calculations were performed under concurrent and countercurrent flow for a hydrogen or methane-fueled planar cell with the following parameters: anode and cathode thickness $\delta_a = \delta_c = 50\ \mu m$, electrolyte thickness $\delta_e = 150\ \mu m$, channel width $W_{ch} = 3$ mm, channel depth $D_a = D_c = 1$ mm, rib width $W_{rib} = 2.42$ mm, total bipolar plate depth $D_{t,a} = D_{t,c} = 2.5$ mm, channel length $L = 100$ mm, and the number of channels $n_{ch} = 18$. For both H_2–H_2O and pre-reformed methane fuel systems, the operating pressure is 1 bar, the air and fuel inlet temperature is 900 °C,

Table 2
Validation of distributed cell model with interface-type PEN model for 90% H_2–10% H_2O fuel mixture.

Parameter	IEA Test 1		Simulation			
	Co-flow	Counter-flow	Co-flow		Counter-flow	
			Simple	Detailed	Simple	Detailed
Average current density ($A\,m^{-2}$)	3000.0	3000.0	2996.3	2998.3	3002.7	3006.7
Cell voltage (V)	0.684–0.722	0.689–0.730	0.700	0.696	0.695	0.690
Maximum current density ($A\,m^{-2}$)	3614–3956	7107–8970	3611.0	3553.7	10569.1	8174.8
Minimum current density ($A\,m^{-2}$)	1020–1686	1080–1297	1202.2	1335.5	810.0	840.6
Maximum solid temperature (K)	1331–1371	1335–1358	1352.2	1344.2	1375.1	1340.1
Minimum solid temperature (K)	1172–1243	1177–1187	1204.3	1194.8	1184.5	1183.9
Maximum solid temperature gradient ($K\,mm^{-1}$)	1.88–2.50	2.90–4.40	2.104	2.085	3.477	−4.463
Fuel outlet temperature (K)	1321–1355	1179–1337	1351.8	1343.7	1184.7	1184.2
Air outlet temperature (K)	1321–1355	1334–1355	1351.0	1343.0	1368.4	1330.1
Cell power (W)	20.52–21.67	20.65–21.89	20.974	20.868	20.869	20.746

the air stoichiometry is $\lambda_{air} = 7$, and the overall fuel utilization is $U_f = 85\%$.

7.2. Fuel system of 90% H_2–10% H_2O

Table 2 shows the validation of the distributed cell model combined with the INT-type PEN model in the base case of 90% H_2–10% H_2O fuel mixture. The values of the main parameters are listed in Table 3.

In Table 2, "detailed" means the detailed numeration of radiant heat transfer with the analytical view factors as mentioned above, while only the radiant heat transfer between two opposing elements is considered in the "simple" numeration. For an assumed enclosed system of PEN–CON rectangle, the "simple" radiation heat flux from PEN element surface to the interconnector element surface can be described as

$$q_{PEN,k} = \frac{\sigma_B(T_{PEN}^4 - T_{CON}^4)}{1/\in_{PEN} + W_{ch}(1/\in_{CON} - 1)/(W_{ch} + 2D_k)} \quad (k=a, c) \qquad (64)$$

Fig. 7 shows the distribution of the current density and solid temperature under both co-flow and counter-flow conditions, which is consistent with the results of IEA Benchmark Test 1 (Figs. 6–9 in Ref. [30]). Under the co-flow condition as shown in Fig. 7(b), the solid temperature predicted by "detailed" calculation was almost 10 K lower than the "simple" calculation. More importantly, the smaller solid temperature gradient (shown in Table 2) implies a more uniform description of the solid temperature from the "detailed" prediction than from the "simple" prediction. Under the counter-flow condition as shown in Fig. 7(d), there is an obvious nonlinear distribution of the solid temperature in the "detailed" calculation. By considering the strong radiant heat loss to the environment in the "detailed" calculation, the maximum negative gradient of the solid temperature appears at the spot close to the fuel inlet. Compared to the "simple" calculation, the "detailed" calculation avoids the overestimation of maximum current density and solid temperature (especially under counter-flow condition), which provides a more uniform distribution of the current density as shown in Fig. 7(a) and (c).

Fig. 8(a) and (c) display the distribution of gaseous and solid temperatures under co-flow and counter-flow conditions. There is sufficient convective heat transfer between gases and solid matrix due to the small flow duct size. Thus the gaseous temperatures are almost identical to the solid temperatures in the major section of the flow channels. As shown in Fig. 8(b) and (d), the distribution of the open circuit voltage is dominated by the fuel concentration under both co-flow and counter-flow conditions. For the electrolyte-supported experimental cell, the cathodic and ohmic overpotential are the main polarizations. Fig. 8(e) shows the distribution of H_2 and O_2 in the anode and cathode flow channels respectively. As shown in Fig. 8(f), there is about a 10% variation of gaseous velocity, which increases with a longer flow channel.

The distributed cell models combined with the CV-type PEN model and its approximate analytical solution (Eq. (34)) were also validated for the H_2–H_2O binary fuel system. For the CV-type PEN model, the electrochemical reaction rates in the anode and cathode were fitted as $i_{0,H_2,ref} S_{TPB,an} = 1.2 \times 10^8\,A\,m^{-3}$ and $i_{0,O_2,ref} S_{TPB,ca} = 0.6 \times 10^8\,A\,m^{-3}$, and the other parameters were the same as those in Table 3. As shown in Fig. 9, there is little difference among the distributions of the current density and overpotentials of INT-type, CV-type, and approximate calculations.

The distributed cell models with the advanced PEN model were also calculated. Here, the activation energy of absorption was $Q_{H_2} = 0.45\,eV\,mol^{-1}$, $Q_{H_2O} = 0.5\,eV\,mol^{-1}$, and the H_2 surface diffusivity at zero and full coverage were $D_{s,H_2,0} = D_{H_2,H_2O}\varepsilon_a/\tau_a/2$ and $D_{s,H_2,1} = D_{H_2,H_2O}\varepsilon_a/\tau_a/200$ [20]. The mechanism of surface diffusion and competition absorption was found to have little effect on the cell performance due to the small resistance of mass transfer as a result of high operating temperature and the small thickness of the anode in the experimental cell. The local current density was far less than the corresponding limit current density (10^6–$10^7\,A\,m^{-2}$). On the other hand, for a set of unit cells in series, the overall fuel utilization was related to the local fuel utilizations

$$U_{f,i} = 1 - \frac{(c_{t,a} u_a x_{H_2})_{i,out}}{(c_{t,a} u_a x_{H_2})_{i,in}} \Rightarrow U_f = 1 - \frac{(c_{t,a} u_a x_{H_2})_{n,out}}{(c_{t,a} u_a x_{H_2})_{1,in}} = 1 - \prod_{i=1}^{n}(1 - U_{f,i}) \qquad (65)$$

Table 3
Parameters of distributed cell model with interface-type PEN model.

Parameter	Symbol	Value
Anode porosity/tortuosity	ε_a/τ_a	0.5/3
Cathode porosity/tortuosity	ε_c/τ_c	0.5/3
Solid heat conductivity ($W\,m^{-1}\,K^{-1}$) [30]	κ_{PEN}, κ_{CON}	2
Solid heat capacity ($J\,kg^{-1}\,K^{-1}$) [30]	$c_{p,PEN}$, $c_{p,CON}$	400
Solid density ($kg\,m^{-3}$) [30]	ρ_{PEN}, ρ_{CON}	6600
Solid emissivity [30]	$\in_{PEN}$, $\in_{CON}$	0.8
Reference H_2 exchange current density ($A\,m^{-2}$)	$I_{0,H_2,ref}$	5800
Reference O_2 exchange current density ($A\,m^{-2}$)	$I_{0,O_2,ref}$	2600
Anode activation energy ($J\,mol^{-1}$) [18]	E_{an}	1.1×10^5
Cathode activation energy ($J\,mol^{-1}$) [18]	E_{ca}	1.6×10^5
Anodic transfer coefficient in the anode [18]	α_a	0.5
Cathodic transfer coefficient in the anode [18]	β_a	0.5
Anodic transfer coefficient in the cathode [18]	α_c	0.5
Cathodic transfer coefficient in cathode [18]	β_c	0.5
H_2 reaction order [18]	γ_{H_2}	0.25
H_2O reaction order [18]	γ_{H_2O}	0
O_2 reaction order [18]	γ_{O_2}	0.25

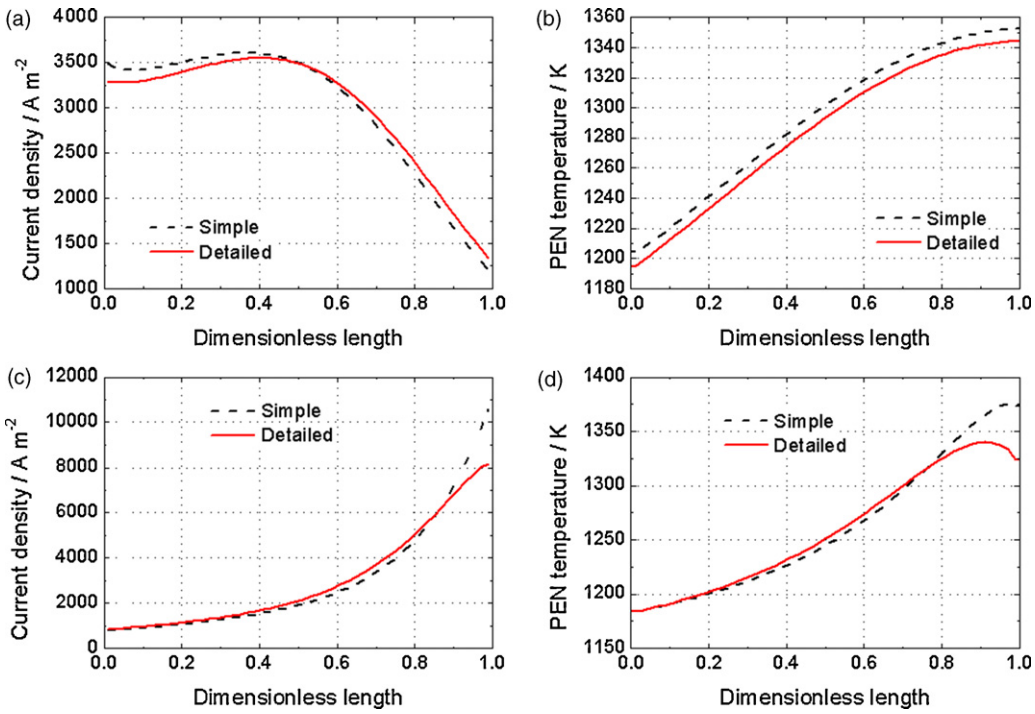

Fig. 7. Distribution of the current density and solid temperature in interface-type calculation. (a) and (b) under co-flow condition, (c) and (d) under counter-flow condition. Both for 90% H_2–10% H_2O fuel system.

As shown in Fig. 10(a), all the local fuel utilizations are smaller than 9%, while the overall fuel utilization is 85%. Therefore, the resistance of surface diffusion was negligible because of its small local fuel utilizations. Furthermore, this was also the idea of stack stage. Fig. 10(b) shows the similar distribution of H_2 molar fraction and H_2 relative coverage at the anode/electrolyte interface under the co-flow condition.

Notice that both the INT-type and CV-type computation failed to show the superior performance of the counter-flow design compared to the co-flow design, which was not consistent with the results given by the IEA models [30]. Ref. [31] explained a similar contradiction that only the one-dimensional effects were taken into account. On the other hand, parameters in a current–overpotential expression (such as the exchange current density, H_2 reaction order, etc.) play an important role for cell performance. For example, when Iwata's data [16] was used, i.e. $i_{0,H_2,ref}S_{TPB,an} = 5.2 \times 10^7\ A\,m^{-2}$, $i_{0,O_2,ref}S_{TPB,ca} = 3.6 \times 10^7\ A\,m^{-2}$, $E_{an} = 138\ kJ\,mol^{-1}$, $E_{ca} = 136\ kJ\,mol^{-1}$, $\gamma_{H_2} = -0.3$, $\gamma_{H_2O} = -0.3$, $\gamma_{O_2} = -0.5$, $\alpha_a = 1$, $\beta_a = 0.5$, $\alpha_c = 1$, and $\beta_c = 1$, the counter-flow design performed better ($I_{avg} = 2950\ A\,m^{-2}$, $V_{cell} = 0.7\ V$) than the co-flow design ($I_{avg} = 2930\ A\,m^{-2}$, $V_{cell} = 0.7\ V$). Similar results can be obtained by using Nagata's data [15], where the negative H_2 reaction order ($\gamma_{H_2} = -0.266$) increased the exchange current density of local unit cells with low H_2 concentrations. Under the counter-flow condition this effect will be more remarkable due to the more non-uniform distribution of current density and fuel concentration.

7.3. Fuel system of 30% pre-reformed methane

Table 4 shows the validation of the distributed cell model combined with the INT-type or CV-type PEN model when 30% pre-reformed methane was used as fuel. For INT-type calculation, Arrhenius's expressions of activation resistance were used to calculate the activation overpotentials, where the pre-exponent factors in Eq. (25) were fitted as 1/1.9 times those in IEA Benchmark Test 2 [30] (i.e. $k_{H_2} = 1.12 \times 10^8\ \Omega^{-1}\,m^{-2}$, $k_{CO} = 1.57 \times 10^8\ \Omega^{-1}\,m^{-2}$, $k_{O_2} = 7.84 \times 10^9\ \Omega^{-1}\,m^{-2}$). For CV-type calculation, the CO electrochemical reaction rate was fitted as

Table 4
Validation of distributed cell model with interface (INT-) type or control volume (CV-) type PEN model for 30% pre-reformed methane. Validation of distributed cell model with interface-type or control volume (CV-) type PEN model for 30% pre-reformed methane.

Parameter	IEA Test 2		INT-type simulation				CV-type simulation			
	Co-flow	Counter-flow	Co-flow		Counter-flow		Co-flow		Counter-flow	
			Simple	Detailed	Simple	Detailed	Simple	Detailed	Simple	Detailed
Average current density ($A\,m^{-2}$)	3000.0	3000.0	3000.0	3000.0	3000.0	3000.0	3003.0	2996.5	2994.5	2999.0
Cell voltage (V)	0.633–0.649	0.680–0.692	0.634	0.650	0.697	0.694	0.661	0.660	0.680	0.675
Max current density ($A\,m^{-2}$)	3040–3665	5330–6554	4067.8	3876.0	6184.3	5758.3	3358.1	3356.6	6525.1	5632.1
Min current density ($A\,m^{-2}$)	1748–2501	994–1332	1841.1	1995.2	897.5	919.8	1774.1	1798.4	947.0	987.2
Maximum solid temperature (K)	1294–1307	1335–1362	1308.7	1312.5	1333.7	1323.1	1300.5	1295.7	1320.2	1304.2
Minimum solid temperature (K)	1100–1135	1179–1188	1134.2	1146.3	1187.4	1186.3	1186.7	1183.7	1190.5	1190.2
Max solid temperature gradient ($K\,mm^{-1}$)	2.2–3.0	6.4–13.3	2.591	2.418	−5.112	−6.359	1.524	1.489	−2.321	−3.082
Fuel outlet temperature (K)	1294–1299	1179–1188	1306.9	1311.1	1187.7	1186.7	1299.6	1294.7	1190.7	1190.5
Air outlet temperature (K)	1289–1299	1291–1301	1305.0	1309.7	1301.3	1278.8	1298.2	1293.5	1306.1	1280.2
Cell power (W)	18.99–19.47	20.40–20.76	19.02	19.50	20.91	20.82	19.85	19.78	20.36	20.24
Inlet fuel component	26.26% H_2–49.34% H_2O–2.94% CO–4.36% CO_2–17.1% CH_4									

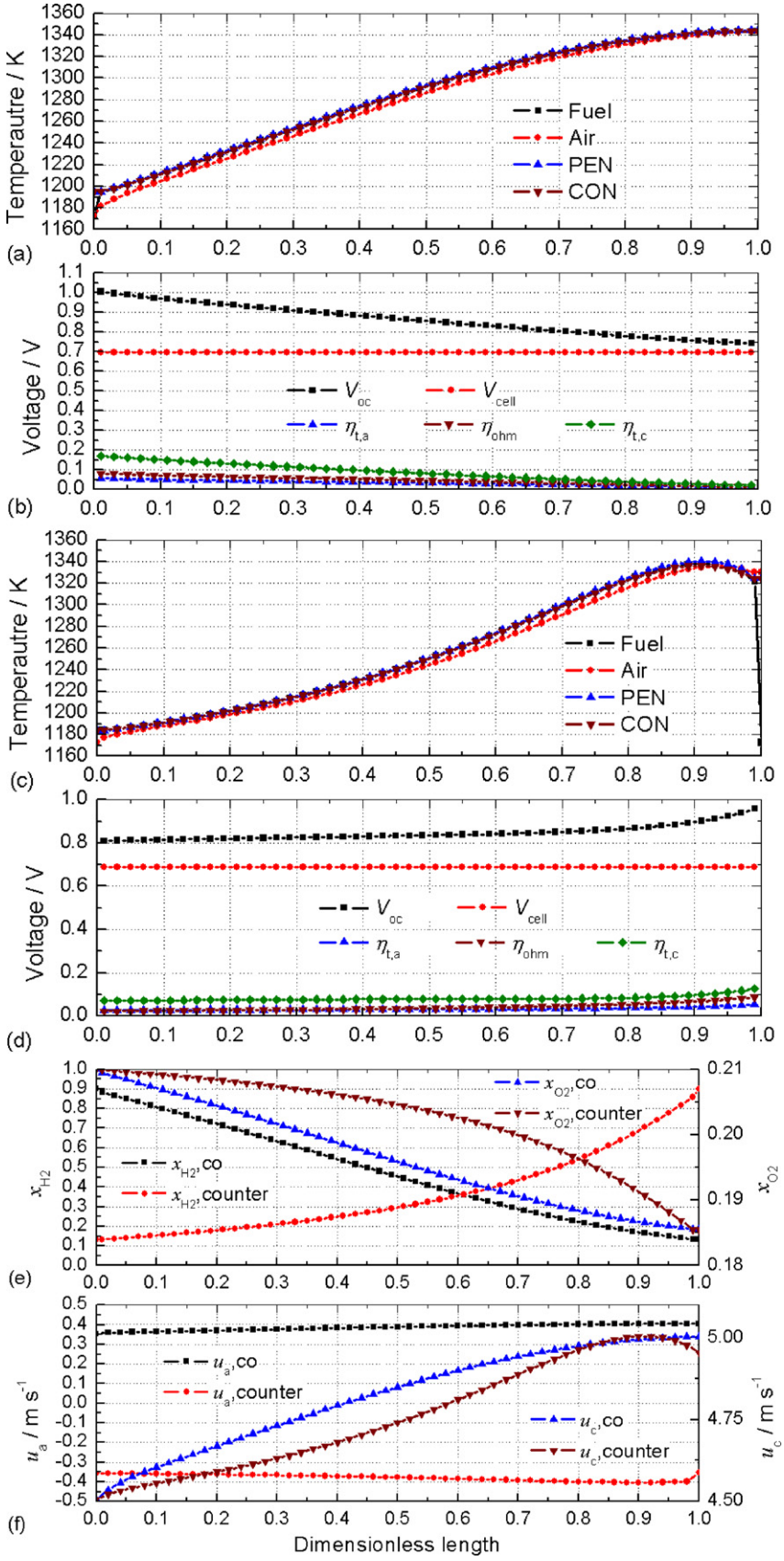

Fig. 8. The temperature distribution of fuel, air, PEN and interconnector under (a) co-flow and (c) counter-flow condition. The distribution of open circuit voltage, cell voltage and overpotentials under (b) co-flow and (d) counter-flow condition. The distribution of (e) H_2 and O_2 molar fraction, (f) fuel and air velocity under co- and counter-flow conditions. All for 90% H_2–10% H_2O fuel system.

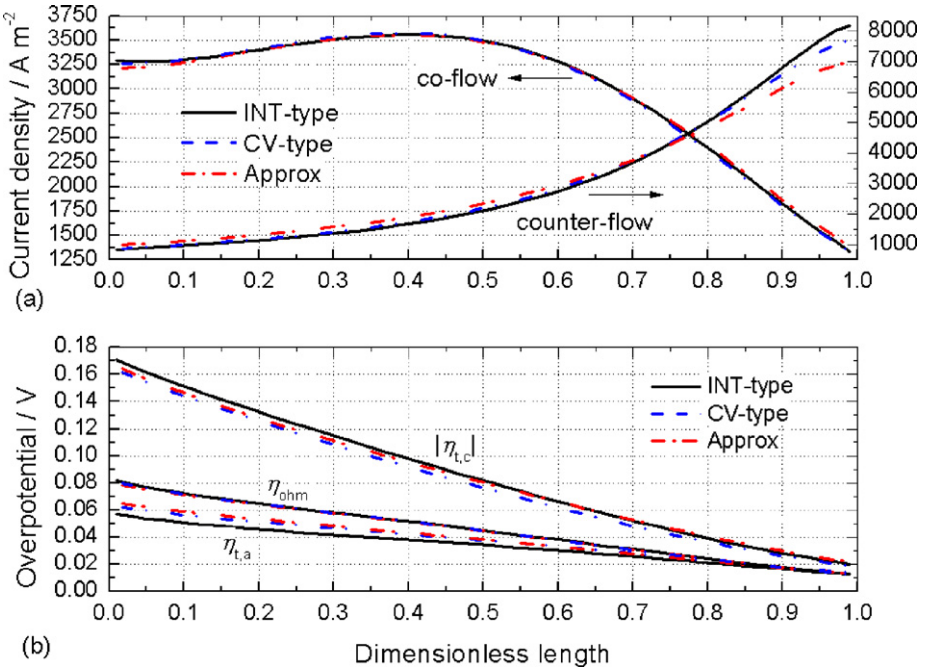

Fig. 9. Comparison among distributed modeling with the interface-type, control volume (CV-) type and approximate analytical PEN model for 90% H_2–10% H_2O fuel system. (a) Distribution of current density under both co-flow and counter-flow conditions, (b) distribution of anodic, cathodic and ohmic overpotential under co-flow condition.

$i_{0,CO,ref}S_{TPB,an} = 1.0 \times 10^8\ A\,m^{-3}$. The other parameters (except the reference exchange current densities) were the same as those in Table 3.

Fig. 11 shows the distribution of the current density and solid temperature under co-flow and counter-flow conditions. With the same structure of electrochemical kinetics, the INT-type calculation was consistent with the results of IEA Benchmark Test 2 (Figs. 14 and 15 in Ref. [30]). For the methane-fueled system, the cell performance was always superior under countercurrent flow than that under concurrent flow. The distributions of current density and solid temperature from the "detailed" calculation were more uniform than those from the "simple" calculation. Similar to the results of the H_2–H_2O fuel system, the maximum solid temperature and cell performance in the "detailed" calculation were generally lower than the "simple" values. However, the INT-type "detailed" cell performance under co-flow condition was exceptionally higher than the INT-type "simple" performance, due to the higher distribution of "detailed" solid temperature as shown in Fig. 11(b). As shown in Fig. 11(d), there are obvious non-monotonic distributions of solid temperature in both the "simple" and "detailed" calculation under counter-flow conditions because of the strongly endothermic methane reforming reaction. By considering the radiant heat loss to the environment, the "detailed" calculation led to a more intense negative gradient of solid temperature at the zone close to the fuel

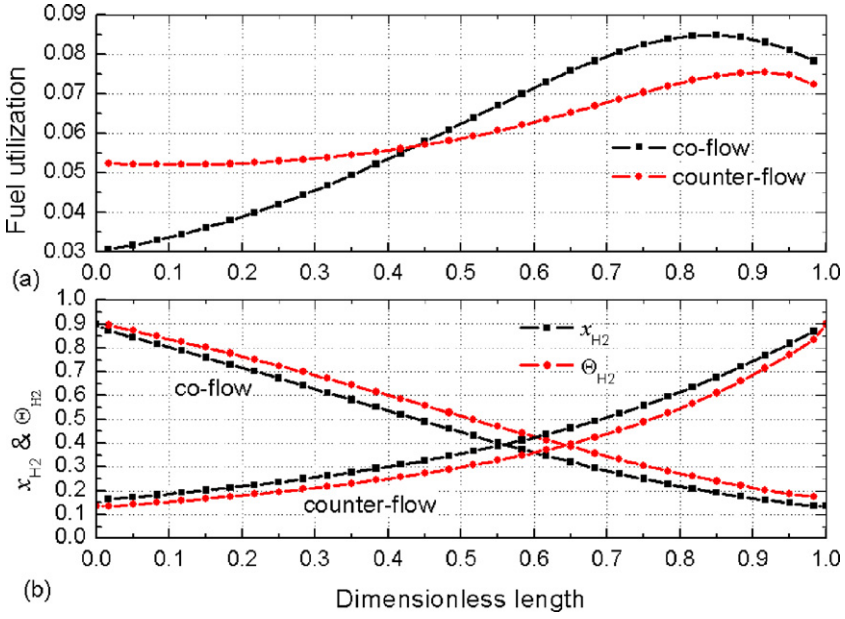

Fig. 10. (a) Distribution of local fuel utilization under co- and counter-flow conditions, (b) distribution of H_2 molar fraction and H_2 relative coverage at the anode/electrolyte interface under co-flow condition. Both for 90% H_2–10% H_2O fuel system.

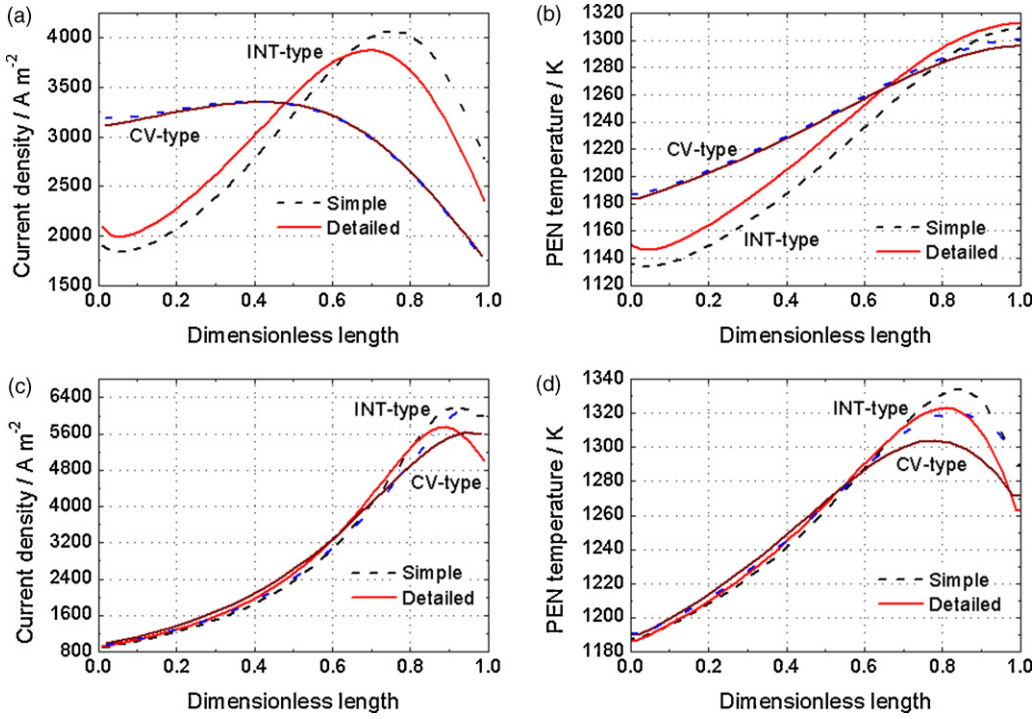

Fig. 11. Distribution of the current density and solid temperature with interface-type and control volume (CV-) type PEN models for 30% of the pre-reformed methane-fueled system. (a) and (b) under co-flow condition, (c) and (d) under counter-flow condition.

inlet. As a result, Fig. 11(c) shows a nonlinear distribution of the current density in both INT-type and CV-type "detailed" calculation.

It is worthwhile to note that Fig. 11(a) shows a large contrasting distribution of current density between INT-type and CV-type calculation under co-flow conditions. This was mainly due to their different descriptions of reforming kinetics. It was found that the INT-type reforming rate per unit area (Eq. (41)) led to a more intense methane conversion than the CV-type volumetric reforming rate (Eq. (18)). Fig. 12(a)–(d) compares the distribution of fuel gas molar fractions between INT-type and CV-type calculations. As shown in Fig. 12(a), most of the methane is converted within the first 10% of the anode flow channel, which leads to the obvious increase of H_2/CO and decrease of H_2O in this section. Afterwards, H_2/CO decreases and H_2O/CO_2 increases because of the electrochemical reaction. However, the CV-type calculation predicts that methane is not fully converted in the first 70% of the flow channel as shown in Fig. 12(b). As a result, there is no obvious increase of H_2/CO and decrease of H_2O close to the fuel inlet, and variations of the fuel component concentration are dominated by the electrochemical reaction. Therefore, Fig. 11(a) shows a similar distribution of the current density as the result of the H_2–H_2O fuel system in Fig. 7(a). On the other hand, Fig. 12(d) also shows a monotonic variation of the fuel gas molar fractions in the CV-type calculation, which results from the stronger electrochemical and reforming reaction close to the fuel inlet under counter-flow conditions. Compared to the CV-type computation, the INT-type calculation also shows a much sharper variation of gas concentrations in Fig. 12(c).

The variation of gas concentrations in the CV-type calculation can be further analyzed from the distribution of the fuel component flux at the anode/channel interface. In this case, the species flux included both the electrochemical flux and chemical flux. As shown in Fig. 12(e) and (f), a negative H_2/CO flux denotes inflow from the anode because of the reforming reaction, while a positive H_2/CO flux indicates outflow from the flow channel because of the electrochemical reaction. Under counter-flow conditions, the H_2 flux close to the fuel inlet is considerable compared to the other species flux. Fig. 12(d) shows a monotonic distribution of H_2 concentration.

Fig. 13(a) shows the distribution of the fraction of H_2 electrochemical current in the total current (ω). In the above Arrhenius-type calculation, the CO electrochemical kinetics is higher than the H_2 electrochemical kinetics ($k_{CO} > k_{H_2}$) [18,30]. In the electrochemical calculation by Butler–Volmer (BV) equation, the reference exchange current density of CO was chosen as $I_{0,CO,ref} = 5000\,A\,m^{-2} < I_{0,H_2,ref}$. Thus, the fraction of H_2 current in the BV calculation was larger than in Arrhenius's calculation. As shown in Fig. 13(b), compared to the INT-type calculation, the CV-type calculation also shows a slower variation of gas velocities because of its smoother reforming kinetics.

Table 5
Comparison among quasi-equilibrium, CSTR and distributed cell-level modeling with interface-type PEN model. Comparison among simulations of quasi-equilibrium, CSTR and distributed cell model with interface-type PEN model.

Parameter	90% H_2–10% H_2O				30% pre-reformed CH_4			
	Quasi- equilibrium	CSTR	Distributed (co-flow)	Distributed (counter-flow)	Quasi-equilibrium	CSTR	Distributed (co-flow)	Distributed (counter-flow)
Average current density ($A\,m^{-2}$)	3000.0	3000.0	2998.3	3006.7	3000.0	3000.0	3000.0	3000.0
Cell voltage (V)	0.646	0.646	0.696	0.690	0.613	0.625	0.65	0.694
Average solid temperature (K)	1367.4	1367.4	1285.0	1258.8	1311.6	1309.6	1229.2	1260.5
Fuel outlet temperature (K)	1367.4	1367.4	1343.7	1184.2	1311.6	1309.6	1311.1	1186.7
Air outlet temperature (K)	1367.4	1367.4	1343.0	1330.1	1311.6	1309.6	1309.7	1278.8

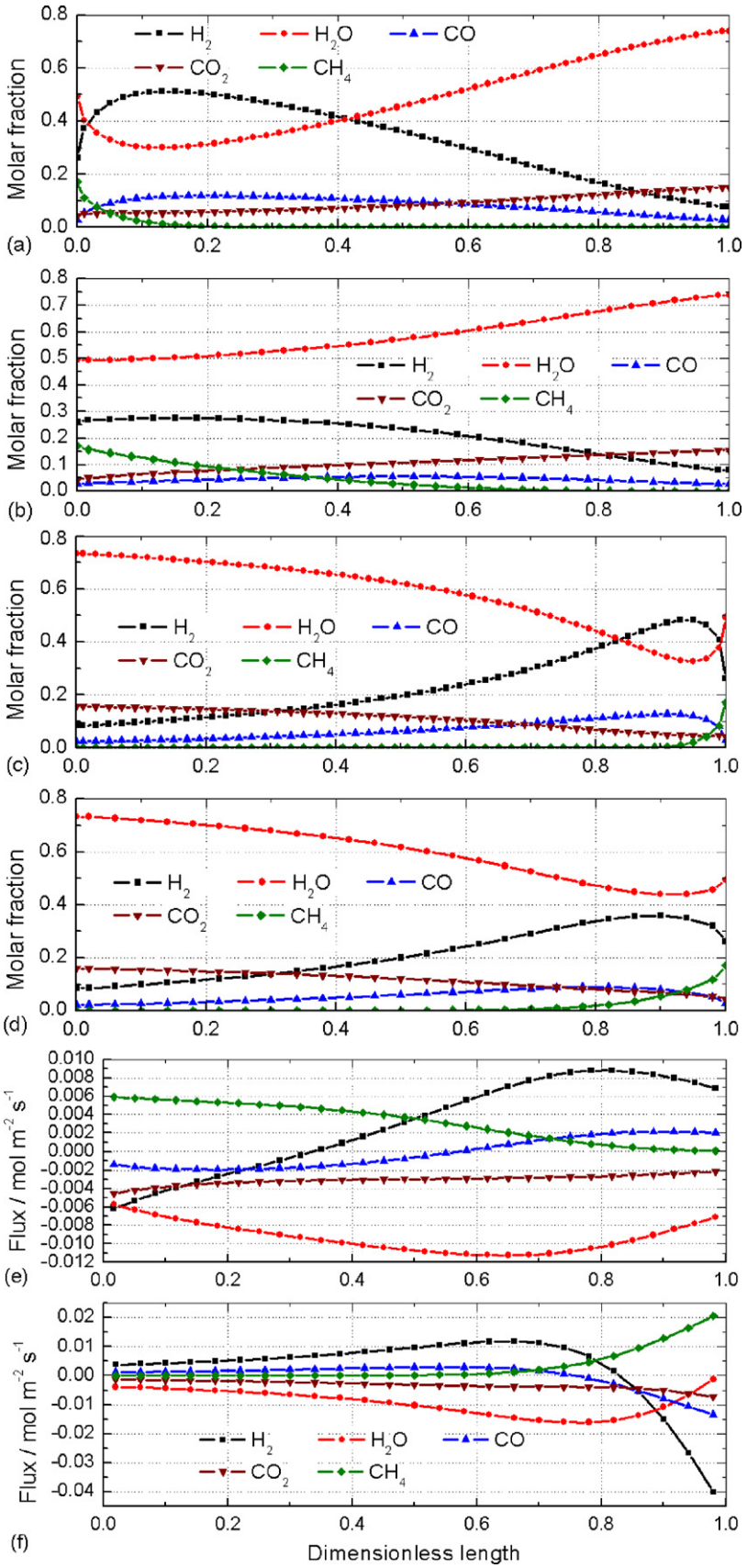

Fig. 12. Distribution of fuel molar fraction under co-flow condition with (a) interface (INT-) type and (b) control volume (CV-) type PEN models. Distribution of fuel molar fraction under counter-flow condition with (c) INT-type and (d) CV-type PEN model. Distribution of species flux through the anode/channel interface with CV-type PEN model under (e) co-flow and (f) counter-flow condition. All for 30% of the pre-reformed methane-fueled system.

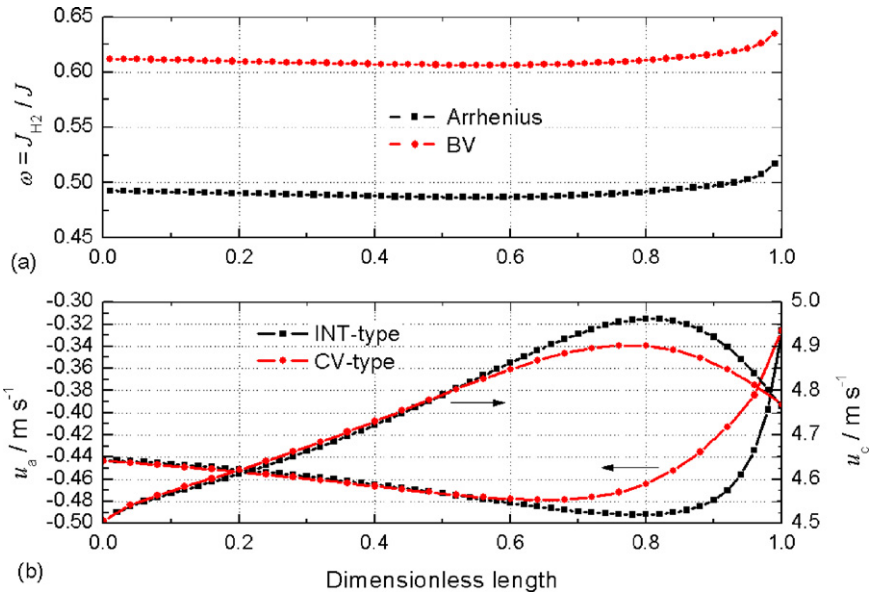

Fig. 13. (a) Distribution of the fraction of H_2 electrochemical current in the total current. (b) Distribution of fuel and air velocity under counter-flow condition. All for 30% of the pre-reformed methane-fueled system.

7.4. Comparison between distributed and lumped calculations

Table 5 shows the comparison among the simulations of quasi-equilibrium, CSTR, and distributed models for H_2–H_2O and methane-fueled systems. With the same electrochemical kinetics, the cell performance from the lumped calculation is generally lower than that from the distributed calculation. This explains why in this paper electrochemical kinetics (k_{H_2}, k_{O_2} or I_{0,H_2}, I_{0,O_2}) lower than the original parameters [30] were chosen to obtain a similar cell power. In the distributed calculation, a significant difference is found between the outlet gas temperatures and the average solid temperature, especially under counter-flow conditions. For SOFC–GT hybrid systems, an adequate prediction of the gas temperatures at SOFC outlets is important for the control of the inlet temperature of the gas turbine. Even under co-flow conditions, there is a significant difference between the average solid temperatures of lumped and distributed calculations. Essentially, the lumped models cannot distinguish the different flow modes.

8. Conclusion

Modeling and simulation plays an important role in the development of SOFC–GT hybrid generation technology. Different system configurations and numerical requirements need multi-level unit models with different complexities. In the first section of this paper, a hierarchical model library of natural gas internal reforming SOFC was presented to reflect the idea of multi-level modeling.

First, two types of general PEN-level models were presented. In the CV-type PEN model, the electrochemical and chemical reactions were considered to occur everywhere at the triple phase boundaries (TPB). In the INT-type PEN model, reactions were assumed to only occur at two ends of the electrodes. For the methane-fueled system, H_2/CO electrochemical polarization and the open circuit voltage of H_2–H_2O–CO–CO_2–CH_4–N_2 mixture were discussed. The different kinetics of reforming and water gas shift reaction in CV-type and INT-type PEN models and the transmission-line analytical model for the ohmic overpotential of tubular SOFC were also introduced.

An advanced electrochemical model was then developed to improve the accuracy of general PEN-level models at high fuel utilization. Based on the diffusion equivalent circuit model, the mechanisms of surface diffusion and competition absorption were introduced to reflect the overall resistance of mass transfer. Via the simple correction of the species concentrations at TPBs, the advanced PEN model kept the same frame and boundary conditions as those of the general PEN models. Furthermore, an approximate analytical solution of the CV-type general PEN model for the binary fuel system was presented based on the perturbation method. As a good balance between mechanistic and semi-empirical calculations, the approximation solution is helpful to the control-oriented modeling and hardware-in-the-loop simulation.

Next, the quasi-equilibrium, lumped dynamic, and distributed dynamic cell-level models were developed. Via a set of unified governing equations for planar and tubular SOFCs, the description of flow and heat transfer in the cell-level models provided the boundary conditions for the isothermal PEN-level models. In the quasi-equilibrium model, reforming and WGS reactions were considered in equilibrium, while flow channels were considered as continuous stirred reactors (CSTR) in the lumped model. In the distributed SOFC model, the variation of the gas velocity, concurrent/countercurrent flow, and detailed radiant heat transfer were considered. The control volume based discretization with the stagger grids was used to solve the numeration problem of discontinuity of the analytical differential view factors. By neglecting the difference between cells, the cell-level model was easily extended for system-level analysis.

(1) In comparison with the IEA Benchmark Test, the multi-level SOFC models in this paper were well validated in both the H_2–H_2O and methane-fueled systems. For the H_2–H_2O system, the cell performance of countercurrent flow was found to be lower than that of concurrent flow. This conflict with the results given by IEA models probably resulted from our one-dimensional modeling. For the methane-fueled system, there was superior cell performance under counter-flow conditions.

(2) Compared to the distributed calculation with “simple” radiant heat transfer, there was a more uniform distribution of the current density and solid temperature in the “detailed” distributed calculation. Besides the INT-type distributed calculation for concurrent flow of the methane-fueled system, the

cell performance predicted by the "detailed" calculation was lower than that predicted by the "simple" one.

(3) By considering the radiant heat loss to the environment, there was generally a non-monotonic distribution of solid temperature in the "detailed" calculation of countercurrent flow. Because of the strongly endothermic reforming reaction in the methane-fueled system, an intense negative gradient of solid temperature appeared near the fuel inlet.

(4) Due to low local fuel utilizations, the mechanism of surface diffusion and competition absorption had little effect on cell performance. This was also the design idea of stack stage.

(5) It was found that the different kinetics of methane reforming reaction led to a more intense conversion of CH_4 in the INT-type calculation than in the CV-type calculation. For the methane-fueled system under co-flow conditions, there was a significant difference between the current density distributions in INT-type and CV-type modeling, which can be further analyzed by the species flux at the anode/flow channel interface in the CV-type calculation.

(6) Compared to the lumped calculation, the distributed calculation showed a more accurate prediction of the average cell temperature and fuel and air outlet temperature, which is important for the control of the SOFC operating temperature and inlet temperature of the gas turbine in SOFC–GT hybrid systems.

(7) A good numeration performance was obtained based on the equation-oriented solver and manual discretization. It took an average of 10 s for the INT-type distributed calculation with 50 grids and 60 s for the CV-type distributed calculation with 30 grids. The relative error of the overall energy balance was less than 0.1%. In the gPROMS commercial environment, all the SOFC models have been specified graphically for modular design in various cases.

In the next part of this research, the multi-level models of other balancing units of the SOFC–GT hybrid generation system will be introduced and the simulation and validation of modeling of tubular SOFC will be introduced.

Acknowledgement

Financial support from the Natural Science Foundation (Project No. 50706019) is gratefully acknowledged. The review performed by Dr. Mark Buck in University of Cambridge is gratefully acknowledged.

Appendix A. Calculation of Gibbs free energy in gPROMS

In the ideal physical properties foreign object (IPPFO) database of gPROMS, the constant pressure molar specific heat is related to the temperature as $C_p = D_1 + D_2/T + D_3T + D_4\ln(T)$. Thus, molar specific enthalpy and molar specific entropy can be calculated by: $H - H_0 = D_1(T - T_0) + D_2\ln(T/T_0) + 0.5D_3(T^2 - T_0^2) + D_4(T\ln T - T_0\ln T_0 - T + T_0)$, $S - S_0 = D_1\ln(T/T_0) - D_2(1/T - 1/T_0) + D_3(T - T_0) + 0.5D_4[(\ln T)^2 - (\ln T_0)^2]$, where, $T_0 = 298.15$ K, H_0 is the molar standard enthalpy of formation, and S_0 is the absolute molar specific entropy at standard condition. For H_2, H_2O, CO, CO_2, CH_4, N_2 and O_2, $S_0 = 130.68$, 188.84, 197.66, 213.79, 186.25, 191.56, 205.07 J mol^{-1} K^{-1}, respectively. The species molar Gibbs free energy can then be obtained from the definition $G = H - TS$.

Appendix B. Differential view factors of PSOFC

The configuration for diffusive interchange in PSOFC is shown in Fig. B1. The view factor between two identical, parallel, and directly opposed finite rectangles ($F_{1,2}$), and the view factor between two finite rectangles of the same length, having one common edge, and 90° from each other ($F_{1,3}$), can be easily found in the view factor catalogue [32].

Define $X = D_{ch}/W_{ch}$, $Z = z/W_{ch}$, $Y = |Z_2 - Z_1|$, and

$$f_1(X,Y) = \frac{1}{2}\ln\frac{Y^2(1+X^2+Y^2)}{(1+Y^2)(X^2+Y^2)} - \frac{X^2}{(X^2+Y^2)^{3/2}}tg^{-1}\frac{1}{\sqrt{X^2+Y^2}} \tag{B1}$$

$$f_2(X,Y) = \frac{1}{2}\ln\frac{(1+Y^2)(X^2+Y^2)}{(1+X^2+Y^2)Y^2} + \frac{X}{(1+Y^2)^{3/2}}tg^{-1}\frac{X}{\sqrt{1+Y^2}} \tag{B2}$$

For the non-concave PEN surface, $dF_{dPEN1,dPEN2} = 0$. According to the reciprocity and additivity rule, the view factor between two infinitesimal elements can be directly calculated from the second-order differentiation of $F_{1,2}$ and $F_{1,3}$

$$dF_{dPEN1,dCON2} = dF_{dPEN1,ds2} = D_{ch}\frac{\partial^2 F_{1,3}}{\partial z_1 \partial z_2}dz_2 = -\frac{1}{\pi}f_1(X,Y)\,dZ_2 \tag{B3}$$

$$dF_{dCON1,dPEN2} = \frac{dA_{PEN,2}}{dA_{CON,1}}dF_{dPEN2,dCON1} = -\frac{1}{\pi(1+2X)}f_1(X,Y)\,dZ_2 \tag{B4}$$

$$dF_{dCON1,dCON2} = -\frac{W_{ch}D_{ch}}{W_{ch}+2D_{ch}}\left(\frac{\partial^2 F_{1,2}}{\partial z_1\partial z_2} + 2\frac{\partial^2 F_{1,3}}{\partial z_1\partial z_2}\right)dz_2 = \frac{2f_2(X,Y)}{\pi(1+2X)}dZ_2 \tag{B5}$$

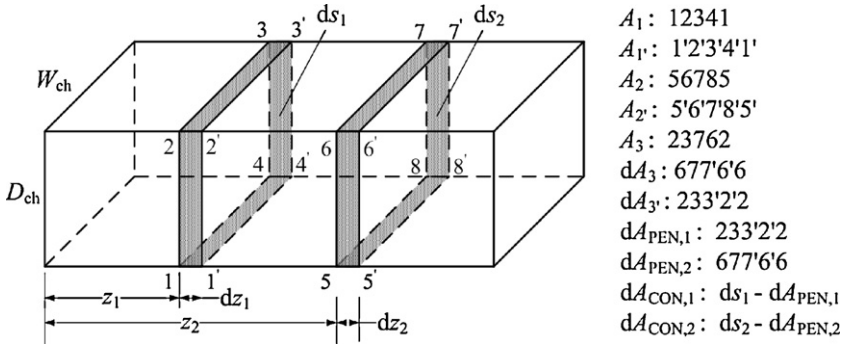

Fig. B1. Configuration for diffuse interchange in PSOFC.

Define

$$f_3(X,Y) = tg^{-1}\frac{1}{Y} - \frac{Y}{\sqrt{X^2+Y^2}}tg^{-1}\frac{1}{\sqrt{X^2+Y^2}} + \frac{Y}{2}\ln\frac{Y^2(1+X^2+Y^2)}{(1+Y^2)(X^2+Y^2)} \quad \text{(B6)}$$

$$f_4(X,Y) = Y\ln\frac{(1+Y^2)(X^2+Y^2)}{(1+X^2+Y^2)Y^2} - tg^{-1}\frac{1}{Y} - X\cdot tg^{-1}\frac{X}{Y} + \frac{Y}{\sqrt{X^2+Y^2}}tg^{-1}\frac{1}{\sqrt{X^2+Y^2}} + \frac{XY}{\sqrt{1+Y^2}}tg^{-1}\frac{X}{\sqrt{1+Y^2}} \quad \text{(B7)}$$

The view factor between the infinitesimal element and the two ends of the groove ($Y_1 = z/W_{ch}$, $Y_2 = (L-z)/W_{ch}$) is related to the first order differentiation of $F_{1,2}$ and $F_{1,3}$

$$F_{dPEN,end} = \frac{D_{ch}}{W_{ch}}\frac{\partial F_{1,3}}{\partial Y}\bigg|_{Y=Y_1,Y_2} = \frac{1}{\pi}[f_3(X,Y_1)+f_3(X,Y_2)] \quad \text{(B8)}$$

$$F_{dCON,end} = \frac{D_{ch}}{W_{ch}+2D_{ch}}\left(-\frac{\partial F_{1,2}}{\partial Y}-\frac{\partial F_{1,3}}{\partial Y}\right)\bigg|_{Y=Y_1,Y_2} = \frac{1}{\pi(1+2X)}\sum_{Y=Y_1,Y_2}(-2f_4-f_3) \quad \text{(B9)}$$

Appendix C. Differential view factors of TSOFC

As shown in Fig. C1, for the configuration of coaxial cylinders, the view factor dFd_{1^*}, d_2 between the differential element (dA_1^*) at the top end of the interior surface of the outer cylinder and the differential annular element (dA_2) on the base of the outer cylinder can be calculated by the contour-integral method [33]. In the cylindrical coordinate system,

$$dF_{d1*,d2} = \frac{1}{2\pi}\oint_{\frown 12+23+\frown 34+41}\frac{y_2-y_1\,dz_2 - z_2 - z_1\,dy_2}{(x_2-x_1)^2+(y_2-y_1)^2+(z_2-z_1)^2} \quad \text{(C1)}$$

where $x_1 = r_2$, $y_1 = 0$, $dz_2 = 0$. For the arc $\frown 12$, $x_2 = r\cos\theta$, $y_2 = r\sin\theta$, $dy_2 = r\cos\theta\,d\theta$, $\theta\in[\theta_m, -\theta_m]$, in which $\theta_m = \cos^{-1}(r_1/r_2)+\cos^{-1}(r_1/r)$. For the line 23, $x_2 = r\cos\theta_m$, $y_2 = -r\sin\theta_m$, $dy_2 = -r_1 r\,dr/r_2/(r^2-r_1^2)^{1/2}$, $r\in[r,\ r+dr]$. Line 41 is symmetric to line 23 along the x axis, and arc $\frown 34$ is in the inverse direction of arc $\frown 21$, as the radius is equal to $r+dr$.

Define $D = r_{in}/r_{AST,out}$, $Z = z/r_{AST,out}$, $H = |Z_2 - Z_1|$, $A = (D+1)^2+H^2$, $B = (D-1)^2+H^2$, then the view factor $F_{dPEN,end}$ between the ring element on the interior of the PEN cylinder and the annular end of channel ($z_2 = 0$, $H = Z$) is

$$F_{dPEN,end} = \int_{r=r_1}^{r=r_2} dF_{d1*,d2} = \frac{1}{\pi D}\left[\frac{2D^2+H^2}{\sqrt{4D^2+H^2}}tg^{-1}\times\frac{\sqrt{(4D^2+H^2)(D^2-1)}}{H} - H\cdot tg^{-1}\sqrt{\frac{D-1}{D+1}} - \frac{(A-2D)H}{\sqrt{AB}}tg^{-1}\sqrt{\frac{A(D-1)}{B(D+1)}} - tg^{-1}\frac{H\sqrt{D^2-1}}{H^2+2(D^2-1)}\right] \quad \text{(C2)}$$

Similarly, the view factor $F_{dAST,out,end}$ between the ring element on the exterior of the AST cylinder and the annular end of the channel ($z_2 = 0$, $H = Z$) is

$$F_{dAST,out,end} = \frac{1}{\pi}\left[H\cdot tg^{-1}\sqrt{\frac{D-1}{D+1}} + tg^{-1}\frac{\sqrt{D^2-1}}{H} - \frac{(A-2D)H}{\sqrt{AB}}tg^{-1}\sqrt{\frac{A(D-1)}{B(D+1)}}\right] \quad \text{(C3)}$$

The view factor between dA_1^* and the exterior surface of the inner cylinder (A_3) and the interior surface of the outer cylinder (A_1), $F_{d1^*,3}$ and $F_{d1^*,1}$, can also be obtained by calculating the line integral along $aa'b'c'cba$ and $deff'e'd'd$ as shown in Fig. C1. The expression of $F_{d1^*,3}$ can be found in the view factor catalogue [32]. Then, the view factors between the ring elements of the PEN and the AST can be obtained by the further differentiation

$$dF_{dPEN1,dAST2,out} = \frac{\partial F_{d1*,3}}{\partial z_2}dz_2 = \frac{1}{\pi D}\left\{\left[1-\frac{H^2(A+B)}{AB}\right]\frac{\sqrt{D^2-1}}{H^2+D^2-1} + \frac{AB(A+B)-16H^2D^2}{2(AB)^{3/2}}tg^{-1}\times\sqrt{\frac{A(D-1)}{B(D+1)}} - tg^{-1}\sqrt{\frac{D-1}{D+1}}\right\}dZ_2 \quad \text{(C4)}$$

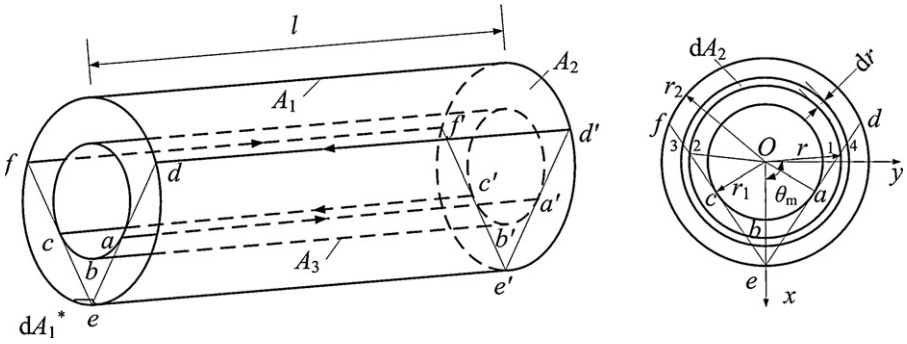

Fig. C1. Configuration for diffuse interchange in TSOFC.

$$dF_{dPEN1,dPEN2,c} = \frac{\partial F_{d1*,1}}{\partial z_2} dz_2 = \frac{1}{\pi D}\left[tg^{-1}\sqrt{D^2-1} - \frac{H(H^2+6D^2)}{(H^2+4D^2)^{3/2}} tg^{-1}\frac{\sqrt{(H^2+4D^2)(D^2-1)}}{H} + \frac{4D^2\sqrt{D^2-1}(H^2+2D^2)}{(H^2+4D^2)[H^2+(H^2+4D^2)(D^2-1)]} - \frac{2\sqrt{D^2-1}}{H^2+4(D^2-1)}\right] dZ_2 \quad (C5)$$

For the non-concave exterior surface of the AST and the PEN, $dF_{dAST1,dAST2,out} = 0$, and $dF_{dPEN1,dPEN2,a} = 0$. With the reciprocity rule, $dF_{dAST1,out,dPEN2} = D.dF_{dPEN1,dAST2,out}$.

The view factor between the ring elements on the interior surface of the AST ($dF_{dAST1,dAST2,in}$) and the view factor of the ring element to the end disk ($F_{dAST,in,end}$) can be obtained by differentiating the view factor of the disk to the parallel coaxial disk. Define $Z = z/2/r_{AST,in}$, $X = |Z_2 - Z_1|$, then

$$dF_{dAST1,dAST2,in} = \left[1 - \frac{X(2X^2+3)}{2(X^2+1)^{3/2}}\right] dZ_2,$$

$$F_{dAST,in,end} = \frac{2X^2+1}{2\sqrt{X^2+1}} - X \quad (C6)$$

Appendix D. Discretization of overall mass balance

Based on the control volume grids as shown in Fig. 6, the overall mass balance (Eq. (50)) can be discretized into $0 = -(J_e - J_w)/\delta z + S_P$, where $J = c_t u T$ is the flux at the west (w) or east (e) interface of the control volume with the center point P, and S_P as the source item.

When defining the convective fluxes as $F_e = (c_t u)_e$ and $F_w = (c_t u)_w$, $J_e - F_e T_P = a_E(T_P - T_E)$ and $J_w - F_w T_P = a_w(T_w - T_P)$. According to the power law or the upwind scheme [27], $(c_t)_e = (c_t)_P$, $(c_t)_w = (c_t)_w$, $a_E = 0$, $a_w = F_w$ for concurrent flow and $(c_t)_e = (c_t)_E$, $(c_t)_w = (c_t)_P$, $a_E = -F_e$, $a_w = 0$ for countercurrent flow. Thus, $J_e - J_w = F_e T_P - F_w T_w$ for concurrent flow and $J_e - J_w = F_e T_E - F_w T_P$ for countercurrent flow.

References

[1] C. Bao, N.S. Cai, Chin. J. Mech. Eng. 44 (2008) 1–7.
[2] A. Bieberle, L.J. Gauckler, Solid State Ionics 146 (2002) 23–41.
[3] W.G. Bessler, Solid State Ionics 176 (2005) 997–1011.
[4] C. Bao, Y.X. Shi, C. Li, N.S. Cai, Q.Q. Su, Int. J. Hydrogen Energy (2009), doi:10.1016/j.ijhydene.2009.05.047.
[5] N.F. Bessette, W.J. Wepfer, J. Energy Resour. Technol. 117 (1995) 307–317.
[6] A.D. Rao, G.S. Samuelsen, J. Eng. Gas Turbines Power 124 (2002) 503–509.
[7] A.F. Massardo, Hybrid system dynamic simulation, in: International Colloquium on Environmentally Preferred Advanced Power Generation, Hybrid Fuel Cell Technologies, Irvine, California, 2005.
[8] P. Heidebrecht, K. Sundmacher, Fuel Cells 2 (2002) 166–180.
[9] Process Systems Enterprise Ltd., gPROMS Advanced User Guide, London, 2004.
[10] P. Aguiar, C.S. Adjiman, N.P. Brandon, J. Power Sources 138 (2004) 120–136.
[11] C. Stiller, Design, operation and control modelling of SOFC–GT hybrid systems, DS Dissertation, Norwegian University of Science and Technology, Trondheim, 2006.
[12] http://www.mathworks.com/products/pde.
[13] Y.X. Shi, N.S. Cai, C. Li, C. Bao, E. Croiset, Q. Hu, J.Q. Qian, S.R. Wang, J. Electrochem. Soc. 155 (2008) B270–280.
[14] B.A. Haberman, J.B. Young, Int. J. Heat Mass Transfer 47 (2004) 3617–3629.
[15] S. Nagata, A. Momma, T. Kato, Y. Kasuga, J. Power Sources 101 (2001) 60–71.
[16] M. Iwata, T. Hikosaka, M. Morita, T. Iwanari, K. Ito, K. Onda, Y. Esaki, Y. Sakaki, S. Nagata, Solid State Ionics 132 (2000) 297–308.
[17] S.H. Chan, K.A. Khor, Z.T. Xia, J. Power Sources 93 (2001) 130–140.
[18] E. Achenbach, J. Power Sources 49 (1994) 333–348.
[19] P.W. Li, M.K. Chyu, J. Heat Transfer 127 (2005) 1344–1362.
[20] C. Bao, Y.X. Shi, C. Li, N.S. Cai, Q.Q. Su, AIChE J. (2009), doi:10.1002/aic.12053.
[21] Y.X. Shi, N.S. Cai, C. Li, J. Power Sources 164 (2007) 639–648.
[22] R.E. Williford, L.A. Chick, G.D. Maupin, S.P. Simmer, J.W. Stevenson, J. Electrochem. Soc. 150 (2003) A1067–A1072.
[23] C. Bao, N.S. Cai, AIChE J. 53 (2007) 2968–2979.
[24] P. Costamagna, P. Costa, V. Antonucci, Electrochim. Acta 43 (1998) 375–394.
[25] E. Achenbach, E. Riensche, J. Power Source 52 (1994) 283–288.
[26] R. Siegel, M. Perlmutter, Int. J. Heat Mass Transfer 5 (1962) 639–660.
[27] S.V. Patankar, Numerical Heat Transfer and Fluid Flow, McGraw-Hill, New York, 1980.
[28] B. Todd, J.B. Young, J. Power Sources 110 (2002) 186–200.
[29] F.P. Incropera, D.P. Dewitt, Fundamentals of Heat and Mass Transfer, fifth ed., Wiley and Sons Inc, 2002.
[30] E. Achenbach, Annex II, Modelling and Evaluation of Advanced SOFC, Subtask A: Numerical Modelling, Experimental Data Base and Validation, Activity A2: Stack Modeling, International Energy Agency, 1995.
[31] J.R. Ferguson, J.M. Fiard, R. Herbin, J. Power Sources 58 (1996) 109–122.
[32] J.R. Howell, A Catalog of Radiation Configuration Factors, McGraw-Hill, New York, 1982.
[33] E.M. Sparrow, R.D. Cess, Radiation Heat Transfer, Rev. ed., Wadsworth, Belmont, CA, 1977.